The DOI for this manuscript is doi: 10.1175/JPO-D-18-0056.1

The final published version of this manuscript will replace the preliminary version at the above DOI once it is available.

# On Internal Waves Propagating Across a Geostrophic Front

Qiang Li, Xianzhong Mao

*Graduate School at Shenzhen, Tsinghua University, Shenzhen, China*

John Huthnance

*National Oceanography Centre, Liverpool, United Kingdom*

Shuqun Cai

*State Key Laboratory of Tropical Oceanography, South China Sea Institute of Oceanology, Chinese Academy of Science, Guangzhou, China*

Samuel Kelly[1]

*Large Lakes Observatory and Department of Physics, University of Minnesota Duluth, Duluth, Minnesota*



[1] *Corresponding author e-mail*: Samuel M. Kelly, smkelly@d.umn.edu

## Abstract

Reflection and transmission of normally-incident internal waves propagating across a geostrophic front, like the Kuroshio or Gulf Stream, are investigated using a modified linear internal-wave equation. A transformation from depth to buoyancy coordinates converts the equation to a canonical partial differential equation, sharing properties with conventional internal-wave theory in the absence of a front. The equation type is determined by a parameter $\Delta$, which is a function of horizontal and vertical gradients of buoyancy, the intrinsic frequency of the wave and the effective inertial frequency, which incorporates the horizontal shear of background geostrophic flow. In the northern hemisphere, positive vorticity of the front may produce $\Delta \leq 0$, i.e., a "forbidden zone", in which wave solutions are not permitted. Thus, $\Delta=0$ is a virtual boundary that causes wave reflection and refraction, although waves may tunnel through forbidden zones that are weak or narrow. The slope of the surface and bottom boundaries in buoyancy coordinates (or the slope of the virtual boundary if a forbidden zone is present) determine wave reflection and transmission. The reflection coefficient for normally-incident internal waves depends on rotation, isopycnal slope, topographic slope and incident mode number. The scattering rate to high vertical modes allows a bulk estimate of the mixing rate, although the impact of internal-waves driven mixing on the geostrophic front is neglected.

## 1. Introduction

Conventional internal-wave theories assume that background vertical stratification ($-\partial B/\partial z$, where $B$ is the buoyancy) is horizontally uniform. However, this assumption is not always valid in the ocean (Fig. 1). Horizontal density gradients are associated with oceanic processes dominated by the geostrophic balance. Intensified jets exist along the western boundaries (e.g., the Kuroshio in the North Pacific Ocean and Gulf Stream in the North Atlantic Ocean), forming a horizontal density gradient that we refer to as a "geostrophic front". Here, we examine internal-wave propagation through horizontal density gradients ($-\partial B/\partial x$) at geostrophic fronts, which act like sloping topography.

Mooers (1975) established a theory for internal-wave propagation inside a geostrophic front. Internal-wave characteristics are distorted by the front due to vertical geostrophic shear. The effective inertial frequency (Mooers 1975; Kunze 1985) is modified by the relative vorticity of the geostrophic front

$$\sigma_f(x,z) = \sqrt{f\left(f + \frac{\partial V}{\partial x}\right)}, \tag{1}$$

where $f$ is the Coriolis frequency and $V$ the background baroclinic current. Cyclonic (anticyclonic) background vorticity increases (decreases) the lower frequency bound of internal waves (Magaard 1968; Mooers 1975; Kunze 1985). Positive vorticity can reflect incoming internal waves, while negative vorticity can enhance wave propagation downward along a chimney-like channel. The group velocity is nearly zero at the base of the front core (i.e., at the chimney mouth), so inertial internal waves are trapped and amplified. Observations of trapped and downward-propagating near-inertial internal waves exist in the North Pacific Subtropical Front (Kunze and Sanford 1984), Gulf Stream warm-core rings (Lueck and Osborn 1986; Kunze

1986; Kunze et al. 1995), the Gulf Stream (Thomas et al. 2016) and other regions (Whalen et al. 2012; Meyer et al. 2015). Internal-wave trapping may enhance local mixing and affect the evolution and fate of the geostrophic front (Kunze et al. 1995; Thomas et al. 2016).

Thermocline tilting at a geostrophic front also affects the generation and propagation of internal tides, which are generated by barotropic tides over sloping topography. For example, the Kuroshio's presence in Luzon Strait produces internal tides with different amplitudes in the South China Sea and Philippines Sea (Buijsman et al. 2010; Li 2014). In an idealized model, Chuang and Wang (1981) find that thermocline shoaling towards a continental shelf suppresses scattering of incident low-mode internal waves to higher modes and inhibits internal-tide generation. In the East China Sea, positive vorticity on the western side of the Kuroshio blocks offshore internal-tide propagation and traps these waves between the shelf break and Kuroshio. As a result, trapped internal-wave beams produce intensified velocity shear (Rainville and Pinkel 2004; Kaneko et al. 2012). Evolving geostrophic fronts and mesoscale eddies also refract horizontally propagating internal tides (Lamb and Shore 1992; Rainville and Pinkel 2006; Zaron and Egbert 2014; Dunphy and Lamb 2014; Kelly and Lermusiaux 2016), producing intermittent internal tides at fixed locations, even when internal-tide generation is steady (Nash et al. 2012). 3D mesoscale eddies also affect internal-wave propagation by shifting the effective inertial frequency, which depends on the kinetic energy of eddies, local buoyancy frequency, and vertical wavenumber of internal waves (Young and Ben-Jelloul 1997).

Waves reflect, refract, or scatter where the properties of their carrier medium change. Horizontally varying stratification alters the internal-wave speed in the same manner as sloping topography. Scattering due to these speed-changes can produce high-mode internal waves that contribute to local mixing, which in turn alters the evolution of the background geostrophic flow (Nikurashin and Ferrari 2013; Wagner and Young 2016).

Most previous studies examined near-inertial internal waves that are generated by wind at the sea surface and propagate downwards (Kunze 1985; Whitt and Thomas 2013; Thomas 2017). Here, we examine internal tides, which are generated by sloping topography and propagate long distances as low vertical modes. We focus on how they reflect and scatter as they cross geostrophic fronts. In section 2, we apply Mooers' (1975) theory to the settings considered by Chuang and Wang (1981). By transforming the internal-wave equation to buoyancy coordinates, we establish a direct analog to classical internal-wave theory. Parameters determining reflection and transmission are analyzed for single-mode incident internal waves in section 3 and for incident rays in section 4. Results from the Kuroshio region are described in section 5. Conclusions and discussion are presented in section 6.

## 2. Analysis

### *2.1 Stability of fronts*

We consider a geostrophic front in an incompressible, inviscid and non-diffusive fluid on an *f*-plane. The Cartesian coordinates are the across-front ($x$), along-front ($y$) and vertical ($z$) positions. The idealized geometry is uniform in $y$ (i.e. 2D) and has a flat bottom and uniform stratification far from the front. The density

$$\rho(x,z,t) = \rho_0\left[1 - g^{-1}B(x,z) - g^{-1}b(x,z,t)\right] \tag{2}$$

includes a background geostrophic buoyancy $B$ and a buoyancy disturbance $b$ caused by internal waves. Here, $\rho_0$ is a constant. The front is stationary, so the background buoyancy is time-independent. The vertical buoyancy frequency is

$$N^2 = \frac{\partial B}{\partial z} \tag{3}$$

and the horizontal buoyancy gradient

$$M^2 = \frac{\partial B}{\partial x}. \tag{4}$$

$M^2$ and $N^2$ can be quantified from in situ observations. $M^2$ is associated with an along-front geostrophic shear via the thermal wind balance. This shear is integrated to yield geostrophic velocity

$$V = \int_{-H_g}^{z} \frac{M^2}{f} dz + V\big|_{z=-H_g}, \tag{5}$$

where, $f$ is the Coriolis frequency, and $H_g$ a reference depth where $V$ is known (or assumed known). $H_g$ is called the "level of no motion" only when $V(H_g)=0$. The ratio between the horizontal and vertical buoyancy frequency

$$S = -\frac{M^2}{N^2} \tag{6}$$

is the isopycnal slope $\partial\xi/\partial x$ where $\xi$ is the vertical isopycnal displacement. Note that $M^2$ can be either positive or negative, depending on the direction of isopycnal shoaling. World Ocean Atlas climatology (Locarnini et al. 2006) provides a global estimate of maximum $|S|$ in the top 100−1000 m (Fig. 1). Large values of $|S|$ coincide with vertical shears in thermal-wind balance, e.g., $|S|$~O($10^{-3}$) in the Kuroshio and O($10^{-2}$) in the Gulf Stream, although the climatology may underestimate actual slopes due to averaging and coarse resolution (0.25°×0.25°).

The front is assumed to be dominated by geostrophic balance, implying that the Rossby number

$$Ro = O\left(\frac{V_x}{f}\right) = \frac{M^2}{fN} \ll 1, \tag{7}$$

so that the absolute vorticity $\zeta = f + V_x$ is always positive in the north hemisphere ($f > 0$). In this case, a stable front requires the balanced Richardson number (Thomas et al. 2013)

$$Ri_B = O\left(\frac{N^2}{V_z^2}\right) = \frac{f^2 N^2}{M^4} = \left(\frac{f}{SN}\right)^2 > \frac{f}{\zeta}. \tag{8}$$

$Ri_B$ indicates the relative importance of buoyancy and shear in the background flow. $Ri_B > f/\zeta$ causes the potential vorticity to be of opposite sign of the Coriolis frequency $f$, leading to inertial or symmetric instability. $Ri_B$ will be used to indicate the stability of fronts in the following analysis. Note that incident internal waves may create instability, turbulence and mixing, even when the background front is initially stable.

### *2.2 Equation for internal waves*

Internal waves normally incident on a 2D geostrophic front $B(x, z)$ are an idealized analog to internal tides propagating across the Kuroshio or Gulf Stream. Normal incidence is a consequence of the 2D idealization. The complexity of realistic 3D flows is not considered. The linearized internal-wave equations within a 2D geostrophic front $B(x, z)$ are

$$\begin{aligned} u_t - fv + p_x &= 0, \\ v_t + fu + uV_x + wV_z &= 0, \\ w_t + p_z - b &= 0, \\ b_t + uM^2 + wN^2 &= 0, \\ u_x + w_z &= 0, \end{aligned} \tag{9}$$

where ($u$, $v$, $w$) denotes wave velocity in ($x$, $y$, $z$) direction and $p=P/\rho_0$ is the reduced pressure perturbation (Gill 1982). Introducing a streamfunction $\psi$, reduces (9) to a single equation (Mooers 1975)

$$\psi_{xxtt} + \psi_{zztt} + N^2\psi_{xx} + \sigma_f^2\psi_{zz} - 2M^2\psi_{xz} = 0. \tag{10}$$

Then, writing the solution as

$$\psi = U_0 H \varphi(x,z)\cdot e^{-i\omega t}, \tag{11}$$

where $U_0$ and $\omega$ are the amplitude and frequency of internal waves, respectively, and $H$ the water depth, the internal-wave equation becomes

$$\varphi_{xx} - \frac{2M^2}{N^2-\omega^2}\varphi_{xz} - \frac{\omega^2-\sigma_f^2}{N^2-\omega^2}\varphi_{zz} = 0. \tag{12}$$

Internal-wave dynamics are influenced by isopycnal slopes $S=-M^2/N^2$ (vertical shears through thermal wind), planetary and relative vorticities (through $\sigma_f$), the intrinsic wave frequency $\omega$ and vertical wavenumber. The boundary conditions

$$\varphi = 0 \text{ at } z = 0 \text{ and } z = h(x). \tag{13}$$

correspond to a rigid-lid and impermeable bottom. Here, $h$ represents the bottom topography. The partial differential equation (PDE) (12) can be hyperbolic, parabolic or elliptic depending on the parameter

$$\begin{aligned}\Delta &\equiv M^4 + (N^2-\omega^2)(\omega^2-\sigma_f^2)\\ &= S^2N^4 + (N^2-\omega^2)(\omega^2 - f^2 + SN^2H_g) \text{ if } M^2 \text{ is } z\text{-independent.}\end{aligned} \tag{14}$$

Kunze (1985) found that positive vorticity can reflect internal waves when $\omega < \sigma_f$. Here, $\Delta$ determines reflection, rather than the relative vorticity, because wave solutions are not allowed by (12) if $\Delta$ is negative. For convenience, we refer to the region with $\Delta$<0 as the "forbidden zone" and the contour $\Delta$=0 as a "virtual boundary". According to (14), $\Delta$ is a function of horizontal and vertical gradients of buoyancy, intrinsic frequency of incident internal waves and background geostrophic shears. Typical conditions in the Kuroshio and Gulf Stream (|$S$| taken from Fig. 1, $N$=0.005 s$^{-1}$, $f$=10$^{-4}$ s$^{-1}$ and $V_x$=±10$^{-5}$ s$^{-1}$) yield $\Delta$>0 for $M_2$ frequency ($\omega$=1.4×10$^{-4}$ s$^{-1}$) so that (12) is hyperbolic (i.e., it permits wave solutions). However, if the local front vorticity $V_x$ exceeds about 10$^{-4}$ s$^{-1}$, a forbidden zone appears, leading to evanescent solutions for (12). Propagation across the geostrophic front is inhibited, although wave tunneling can occur if the forbidden zone is weak or narrow (Bender and Orszag 1978). Negative $\Delta$ can also appear at low latitudes if a front has large vorticity (Kunze 1985; Rainville and Pinkel 2004; Thomas et al. 2016).

Using (9), the phase-averaged energy flux $\mathbf{J}$=($J_x$, $J_z$) is

$$\begin{aligned} J_x &= \langle \psi P_z \rangle \\ &= \frac{\rho_0 U_0^2 H^2}{4i\omega}\left[ M^2(\varphi\varphi_z^* - \varphi^*\varphi_z) - (N^2-\omega^2)(\varphi\varphi_x^* - \varphi^*\varphi_x) \right] \end{aligned} \tag{15}$$

and

$$\begin{aligned} J_z &= \langle -\psi P_x \rangle \\ &= \frac{\rho_0 U_0^2 H^2}{4i\omega}\left[ (\omega^2-\sigma_f^2)(\varphi\varphi_z^* - \varphi^*\varphi_z) + M^2(\varphi\varphi_x^* - \varphi^*\varphi_x) \right]. \end{aligned} \tag{16}$$

Angle brackets represent phase averages and asterisks complex conjugates. For horizontally uniform stratification ($M^2$=0), these formulae revert to conventional expressions (Pétrélis et al. 2006). In the absence of external forcing or dissipation, the phase-averaged energy-flux divergence of monochromatic internal wave is zero, i.e.,

$$\nabla \cdot \mathbf{J} = 0. \tag{17}$$

In the following analysis, we assume that stratification is horizontally uniform ($M^2$=0) in the far field, so that an incident mode-$m$ internal wave with amplitude $A_m$

$$\psi_i = -A_m \sin \frac{m\pi z}{H} e^{i(k_m x - \omega t)}, \tag{18}$$

has vertically-averaged energy flux

$$\overline{J_i} = \rho_0 \frac{\omega^2 - f^2}{2\omega} k_m^{-1} A_m^2. \tag{19}$$

where $k_m$ is the wavenumber and an overbar represents a vertical average. The reflection coefficient $R$ and transmission coefficient $X$ are ratios of the vertically averaged reflected energy flux $\overline{J}_r$ and transmitted energy flux $\overline{J}_t$ to the total incident energy flux $\overline{J}_i$, respectively, i.e.,

$$R = \frac{\overline{J}_r}{\overline{J}_i} \text{ and } X = \frac{\overline{J}_t}{\overline{J}_i}. \tag{20}$$

Equation (12) is solved following Lindzen and Kuo (1969) and validated through comparison with simulations using the MITgcm model (Marshall et al. 1997).

### *2.3 A front example*

Here, we analyze an idealized front

$$M^2 = -sN^2 \operatorname{sech}^2\left(\frac{x}{W}\right), \tag{21}$$

corresponding to the density profile

$$\rho = \rho_0 \left\{1 - g^{-1} N^2 \left[H + z - sW \tanh\left(\frac{x}{W}\right)\right]\right\}. \tag{22}$$

The nominal vertical buoyancy frequency is constant, $N$=5×10$^{-3}$ s$^{-1}$. The maximum isopycnal slope is |$s$| and the width of front $W$. In the MITgcm simulation (Fig. 2), $s$=−0.01and $Ri_B$=4, satisfying the stability condition (8), so the background front is stable. Incident mode-one $M_2$ internal waves with amplitude $U_0$=0.10 m s$^{-1}$ propagate into the domain from the left boundary. Wave currents are small, so wave-wave advection is negligible and the simulation is approximately linear. Other parameters and configurations used in the simulations are listed in Table 1. Normalized wave velocities $u/U_0$ at t=360.7 hr are consistent between the direct solution of (12) and MITgcm (Fig. 2). Two internal wave beams are generated, collinear to the slope of characteristics

$$\alpha^{\pm} = \frac{-M^2 \pm \sqrt{\Delta}}{N^2 - \omega^2} \tag{23}$$

derived from (12) .

Reflected and transmitted internal waves are separated using a Fourier transform, which converts the streamfunction $\varphi$ from the space domain ($x$, $z$) to the wavenumber domain ($k$, $m$). Separate inverse Fourier transforms for positive and negative $k$ isolate waves propagating in opposite directions (Fig. 3), which can be viewed in depth or buoyancy coordinates (buoyancy coordinates are discussed in section 2.5). At the front, wave transmission $X$=97.1% is much larger than reflection $R$=2.9%. In general, reflection is weak for incident waves with long wavelengths in the absence of forbidden zones.

### *2.4 Neglected dynamics*

The derivation of (12) employs several approximations to produce a tractable system with a reduced parameter space. Here, we review the effects of each approximation. The theory formally requires a front with small Rossby number and large Richardson number to ensure a stable and steady geostrophic flow.

Ignored nonlinear effects can cause internal wave steepening or breaking (Farmer 1978) and feedbacks between internal waves and the front (Nagai et al. 2015). In addition, viscosity is neglected so highly sheared internal waves propagate freely without dissipation.

Equation (12) describes 2D dynamics, so interactions between internal waves and 3D background conditions are not retained. Mesoscale eddies or meanders produce 3D advection, dispersion and refraction (Lighthill 1978; Olbers 1981; Klein et al. 2003), resulting in convergence or divergence of internal-wave energy (Rainville and Pinkel 2006; Dunphy and Lamb 2014; Duda et al. 2018). Doppler-shifting is omitted because the idealized geostrophic flow is perpendicular to wave propagation. Rough and complex 3D bathymetric features, such as ridges or canyons, are omitted. The smooth 2D topography may underestimate internal-tide generation (Osborne et al. 2011) and fail to reproduced observed internal tides (Martini et al. 2011; Nash et al. 2012).

Although many wave/mean flow interactions are more complicated than those included in our model (Peters 1983), the model is simple enough that individual parameters can be systematically varied to quantify low-mode internal wave scattering over a broad range of idealized fronts. The model can provide numerically-efficient order-of-magnitude estimates of scattering across many different regions in the ocean. The model may retain some accuracy even when the formal requirements of small Rossby number, large Richardson number and linear internal waves are violated. Therefore, the results reported here could provide a useful complement to less tractable but more realistic 3D nonlinear models of internal waves interacting with unstable submesoscale fronts, provided that the neglected processes do not dominate.

*2.5 Relation to the conventional internal wave equation*

In horizontally uniform stratification, the wave equation takes the canonical hyperbolic form. For horizontally varying stratification the wave equation (12), in the hydrostatic limit, becomes

$$\varphi_{xx} - \frac{2M^2}{N^2}\varphi_{xz} - \frac{\omega^2 - \sigma_f^2}{N^2}\varphi_{zz} = 0. \tag{24}$$

This equation can be rewritten in buoyancy coordinates (*x'*, *B*), where

$$x' = x \text{ and } B = B(x,z), \tag{25}$$

so that the cross-derivative term disappears,

$$\begin{aligned}&\varphi_{x'x'} - \left(\omega^2 - \sigma_f'^{\,2}\right)N^2\varphi_{BB}\\ &\quad = \left[\left(M^2\right)_x + 2\frac{M^2}{N^2}\left(M^2\right)_z + \left(\frac{\omega^2 - \sigma_f'^{\,2}}{N^2} - \frac{M^4}{N^4}\right)\left(N^2\right)_z\right]\varphi_B.\end{aligned} \tag{26}$$

In buoyancy coordinates, the effective Coriolis frequency is

$$\sigma_f'^2 = f(f + V_{x'}), \tag{27}$$

where

$$V_{x'} = V_x - \frac{M^4}{fN^2}. \tag{28}$$

The boundary conditions become

$$\varphi = 0 \text{ at } B = B_s(x') \text{ and } B = B_b(x'), \tag{29}$$

where $B_b$ and $B_s$ represent the bottom and surface, respectively. The sign of

$$\Delta' = (\omega^2 - \sigma_f'^2)N^2, \tag{30}$$

which appears on the LHS of (26), determines whether (26) is hyperbolic, parabolic or elliptic. If $\Delta\,'<0$, (26) is hyperbolic and normal modes and modal wave speeds can be calculated from a plane-wave solution. Although, analytical modal solutions are typically impossible when the coefficients of (26) are functions of ($x'$, $B$). If $M^2$ and $N^2$ are constant, (26) becomes

$$\varphi_{x'x'} - \left(\omega^2 - \sigma_f^{'2}\right) N^2 \varphi_{BB} = 0, \tag{31}$$

which has the same format as the conventional internal-wave equation. Thus, conclusions and methods from conventional internal-wave analysis apply to flows with horizontally varying stratification in buoyancy coordinates. For instance, (31) is a standard hyperbolic equation if $\Delta' > 0$, so it may be solved using normal-mode decomposition (Kelly et al. 2013) or Green's functions (Robinson 1969; Pétrélis et al. 2006; Balmforth and Peacock 2009). The transformation also indicates that a tilted thermocline can be mimicked in a laboratory by implementing appropriate surface and bottom boundaries (i.e., frontal effects can be replicated using topographic bumps in the same way that the beta effect can be replicated using a sloping bottom). Where $M^2$ and $N^2$ are not constant, (26) can be efficiently solved using the method provided by Lindzen and Kuo (1969).

The coordinate transformation (25) reveals equivalent effects of horizontally varying stratification and bottom topography. The wavefield in ($x$, $z$) coordinates shown in Fig. 2 is transformed to the buoyancy coordinates ($x'$, $B$), shown in Fig. 3. In the buoyancy coordinates, the bottom and surface boundaries become

$$B_b = N^2 sW \tanh\frac{x'}{W} \text{ and } B_s = N^2(H + sW \tanh\frac{x'}{W}), \tag{32}$$

respectively. That is to say, even though the surface and bottom boundary are flat in the (*x, z*) coordinates, they are not in the (*x'*, *B*) coordinates. In conventional internal wave theory, beams are emitted from the *critical slope*, at which the characteristics of internal waves are parallel to the bottom and surface boundaries, or from the maximum slope if no critical slope is present. In a geostrophic front, the *effective* slope ratios between the buoyancy coordinate boundaries and the internal wave characteristics are

$$\begin{aligned} \frac{B_{bx}}{\alpha_b} &= \frac{M}{N\sqrt{\omega^2-\sigma_f'^2}} = \pm 1 \text{ at the bottom and} \\ \frac{B_{sx}}{\alpha_s} &= \frac{M}{N\sqrt{\omega^2-\sigma_f'^2}} = \pm 1 \text{ at the surface.} \end{aligned} \tag{33}$$

Critical effective slopes thus indicate locations where beams originate in a geostrophic front. E.g., the boundaries in Fig. 3 do not have critical points, but a reflected (transmitted) beam radiates from the maximum surface (bottom) slope near the center of the front.

## 3. Single-mode propagation

Here, we investigate the propagation of a single-mode internal wave across a geostrophic front. Solutions to (12) are obtained for incident internal waves with $M_2$ tidal frequency ($\omega$=1.4×10$^{-4}$ s$^{-1}$) in a mid-latitude band ($f$=10$^{-4}$ s$^{-1}$). The background front is defined by (22), in which the horizontal buoyancy gradient, $M^2$, varies with *x*, but is constant with depth. The background velocity (34) also depends on the choice of $H_g$ and $V(H_g)$. Here, we arbitrarily set $V(H_g)=0$ m s$^{-1}$ and examine flows where $H_g \in [-H, 0]$. I.e., we only examine results for geostrophic flows that have a level of no motion, even though (12) applies equally to flows without a level of no motion (e.g., Antarctic Circumpolar Current; Damerell et al. 2013). Initial solutions consider a flat bottom, but subsequent solutions include varying topography to illustrate the equivalent effects of horizontally varying stratification and topography. Similarly, initial solutions consider a mode-one incident wave, but later solutions examine high-mode incident waves.

*3.1 Critical slopes and forbidden zones*

The effective Coriolis frequency ($\sigma_f$) and background stratification ($M^2$, $N^2$) determine the sign of $\Delta$ according to (14). Wave solutions are not allowed by (12) for $\Delta \leq 0$. The effective Coriolis frequency depends, in part, on the horizontal geostrophic shear, which in requires the absolute geostrophic velocity (not just thermal wind). Since we arbitrarily set $V(H_g)=0$ m s$^{-1}$, here, the reference level ($H_g$) becomes the level of no motion, which we tune to control the sign of $\Delta$. Most geostrophic flows are wind driven and, therefore, surface intensified with a level of no motion in mid-depth. However, bottom intensified geostrophic currents are also observed (e.g., Bishop et al. 2012), which may correspond to higher levels of no motion.

Some levels of no motion produce an area with $\Delta<0$ (i.e., a forbidden zone). For the front considered here [$V(H_g)=0$ m s$^{-1}$ and (22) with $s=-0.01$ and $W$=25 km], reflection and transmission coefficients vary greatly with $H_g$ (Fig. 4). If 590 < $H_g$ <1410 m, there are no forbidden zones and reflection at the front is weak (Fig. 5b). If $H_g$ < 590 m or $H_g$ > 1410 m, a forbidden zone exists near the bottom (Fig. 5a is for $H_g$ = 0 m) or surface (Fig. 5c is for $H_g$ = 2000 m). If $H_g$ < 725 m or $H_g$ > 1275 m, critical effective slopes (35) appear and create beam-like scattering. Thus, three regimes can be distinguished for the solutions.

*Regime I*: 0 < $H_g$ < 590 m and 1410 < $H_g$ <2000 m

A forbidden zone appears and intersects either the bottom or surface boundary where the slope is critical. Inside the forbidden zone ($\Delta<0$) waves are evanescent, so internal-wave transmission is impeded. If $H_g = 0$ m, a ridge-like forbidden zone near the bottom causes significant reflection at its pinnacle (Fig. 5d). A relatively weak reflected beam also originates from the maximum (subcritical) surface slope. Wave transmission is reduced due to blocking by the forbidden zone, although a transmitted rightward-propagating beam is emitted from the right critical point. If $H_g = 2000$ m, a canyon-like forbidden zone near the surface reflects waves in a highly focused ray that originates from its trough (Fig. 5f). The reflected beam is more diffuse when $H_g = 0$ m than $H_g = 2000$ m, because the ridge-like forbidden zone for $H_g = 0$ m blocks a greater vertical extent of the water column occupied by the incident mode-one wave. Thus, low modes contribute more to the reflected wave field (e.g., Klymak et al. 2013). Because internal wave rays cannot penetrate the forbidden zone or the surface boundary, no transmitted ray forms at the critical points when $H_g = 2000$ m (Fig. 5i).

*Regime II*: $590 < H_g < 725$ m and $1275 < H_g < 1410$ m

Critical slopes occur on either the surface or bottom boundary, but there are no forbidden zones, so reflection is weaker than in Regime I. Scattering occurs near the critical slope. If critical slopes occur on the bottom boundary, a transmitted ray is emitted from the bottom and a reflected ray from the maximum (subcritical) surface slope.

*Regime III*: $725 < H_g < 1275$ m

Both surface and bottom boundaries are subcritical and there are no forbidden zones, so wave reflection is very weak. Scattering is similar to the cases in Regime II, but the emitted rays are weaker and originate from the maximum (subcritical) slopes (Fig. 3). This $H_g$ regime is most typical of the Kuroshio or Gulf Stream.

In summary, forbidden zones significantly affect wave reflection and transmission. Total transmission (reflection) increases (decreases) with $H_g$ for $H_g$ < 1000 m and then decreases (increases) for $H_g$ > 1000 m (Fig. 4a). The transmitted energy flux of a mode-one wave is symmetric with respect to $H_g$ = 1000 m (Fig. 4b), and only determined by the minimum effective vertical thickness of the waveguide. For example, for $H_g$ = 0 m and 2000 m, the vertical scales of forbidden zone are equal, so the effective vertical thicknesses of the waveguides are the same.

High-mode energy fluxes are asymmetric with respect to $H_g$. A level of no motion at the surface causes stronger reflection than at the bottom. If the level of no motion is near the surface, the rightward-shoaling surface boundary and forbidden zone reflect high-mode waves (Fig. 5d). High-mode wave transmission increases with $H_g$ (Fig. 4c) because the slope ratio between the bottom boundary and upward-transmitted ray increases with $H_g$.

### *3.2 Effect of isopycnal slope*

Here we investigate internal-wave reflection and transmission across fronts with different horizontal buoyancy gradients. Solutions are presented for incident mode-one internal waves at the $M_2$ tidal frequency, and a front with $V(H_g)=0$ m $s^{-1}$ and $H_g$ = 2000 m. In this case, the bottom boundary is always subcritical, i.e.,

$$B_{bx} = -M^2 < \sigma\big|_{B=B_b}, \tag{36}$$

However, the surface boundary has critical slopes and a forbidden zone for large $|s|$. We choose a front width $W$ = 25 km, so $s \in [-0.05, 0.05]$ determines the isopycnal slope. Note that $|s| \geq 0.02$ may not be realistic in the ocean where climatology indicates $|S| \sim O(10^{-5}\text{-}10^{-2})$ (Fig.1)

A large horizontal buoyancy gradient $M^2$ enhances interaction between internal waves and the buoyancy-coordinated boundaries, i.e., transmitted energy flux decreases and reflected energy flux increases with increasing isopycnal slope (Fig. 6). Since we set $V=0$ at the bottom, the surface buoyancy boundary dominates the interaction with internal waves. Reflection and transmission coefficients are asymmetric for $s$ such that reflected waves are stronger for rightward shoaling stratification ($\partial\xi/\partial x>0$) than for leftward shoaling ($\partial\xi/\partial x<0$). E.g., for small $s$ (i.e., no forbidden zone or critical slopes), internal waves encountering a downward sloping surface boundary experience stronger reflection than those encountering an upward sloping surface boundary because the downward sloping surface boundary directly blocks internal-wave propagation. This situation is analogous to internal waves propagating across a continental shelf, in which reflection for shoreward propagating internal waves is stronger than for seaward propagating waves (Chapman and Hendershott 1981).

A forbidden zone appears for $s<0$ but not for $s>0$. If a forbidden zone exists, the virtual boundary increases the contact slope for interaction between internal waves and the surface boundary. For $s=0.01$, energetic reflected beams emanate from the surface forbidden zone (Fig. 7).

In summary, the shoaling direction of the surface buoyancy boundary and locations of the forbidden zone produce asymmetric total reflection and transmission coefficients (Fig. 6a). Transmission of mode-one internal waves is related to the ratio between their vertical wavelength and thickness of waveguide channel, which can be less than the water depth due to a forbidden zone. Energy transmission in mode-1 alone is symmetric in $s$ (Fig. 6b), but higher-mode transmission is asymmetric. There is almost no high-mode transmission for $s>0$, while high-mode transmission is significant for $s<0$ because the incident wave scatters off the bottom buoyancy boundary, which shoals to the right.

High-mode reflection increases with horizontal buoyancy gradients (Fig. 6d). For $s>0$, the beam reflected from the surface or forbidden zone propagates downward and arrives at the tilted bottom buoyancy boundary, which causes secondary scattering and enhances energy transfer to high modes. No further scattering takes place for $s$<0 because the bottom buoyancy boundary is flat where the downward reflected beam hits. For $s$<0, the reflected energy flux in each mode increases with |$s$|. For $s$>0, the reflected energy flux in each mode is maximum at a value of $s$ that increases with mode number.

An offshore propagating mode-one wave that crosses a western boundary current is likely to scatter into high-mode waves that are transmitted, while an onshore-propagating mode-one wave is likely to scatter into high-mode waves that are reflected (Fig. 6d). For the latter case, the energy flux of transmitted high-mode waves is nearly zero.

In the East China Sea, the continental shelf and Kuroshio may form an attractor so that part of offshore propagating internal-wave energy is trapped between them, thus enhancing local mixing as observed by Rainville and Pinkel (2004).

### *3.3 High-mode incident waves*

Reflection coefficients can increase or decrease with incident-mode number, depending on $s$ (Fig. 8a), when the front is defined by (22) with a width of $W$ = 25 km. In the far field, the bottom is flat and stratification uniform (i.e., $N^2$=const. and $M^2$=0), so horizontal and vertical wavelengths of the incident internal waves are inversely proportional to mode number $m$, i.e.,

$$\lambda_m^{(H)} = \frac{2H}{m}\sqrt{\frac{N^2-\omega^2}{\omega^2-f^2}} \text{ and } \lambda_m^{(V)} = \frac{2H}{m}, \tag{37}$$

respectively. For $s$=±0.005 ($Ri_B$=16), the surface and bottom buoyancy boundaries are subcritical and no forbidden zone exists. Reflection decreases with increasing mode number because incident waves with $\lambda_m^{(H)} < 2W$ (equivalent to $m$>4) cannot *sense* the horizontal buoyancy gradient $M^2$ (so the reflection coefficient is nearly zero). For $s$=±0.01, a forbidden zone, with vertical thickness $H_\Delta$ = 591 m, forms near the surface and blocks part of the waveguide, reflecting high-mode internal waves. Reflection increases with mode number until $\lambda_m^{(V)} \leq 2H_\Delta$ (equivalent to $m$>3), at which reflection becomes constant with mode number. For all modes, reflection for $s$=+0.01 is greater than for $s$=−0.01 due to additional reflection from the surface buoyancy boundary (section 3.2). In summary, if $\Delta > 0$ (e.g., $s$=±0.005), high-mode reflection decreases with mode number, because their horizontal wavelengths are short compared to the width of the front. However, if $\Delta < 0$ (e.g., $s$=±0.01), high-mode waves with short vertical wavelength are partially blocked by the forbidden zone, and reflection increases with mode number.

The forbidden zone also creates a ``shadow'' in its lee by blocking internal-wave rays (Fig. 8b-d). For mode-8 internal waves, a shadow appears on the top where the high-mode internal waves are blocked by the forbidden zone. A second shadow appears near the bottom right of the front because the bottom buoyancy boundary is tilted (Fig. 8d), which causes transmitted waves to propagate upwards.

### *3.4 Interaction between stratification and topography*

Both horizontal buoyancy gradients and sloping topography reflect internal waves. Their joint effects are discussed in this section. The bottom topography is

$$h = -H + \beta s W (1 + \tanh\frac{x}{W}), \tag{38}$$

in which the coefficient $\beta$ indicates the ratio between bottom and isopycnal slopes. If $\beta$=1, the bottom topography is collinear with the isopycnals defined in (22). Incident mode-one waves are prescribed, propagating from left to right. When $\beta s$>0 ($\beta s$<0), the setup is analogous to onshore (offshore) wave propagation across a shelf break. The sea surface $\eta$ is assumed to be parallel to the stratification, i.e.,

$$\eta = sW(1 + \tanh\frac{x}{W}), \tag{39}$$

so that the surface is flat in buoyancy coordinates. The geostrophic velocity is $V(H_g)$=0 m s$^{-1}$ at $H_g$=0 m. Although this profile is not observed in the ocean, it is convenient here because it eliminates interactions between internal waves and stratification near the surface, so reflection and transmission are determined solely by the bottom slope (Fig. 9). Because of the front, scattering transfers energy to high modes even when the boundary is flat, and scattered waves propagate as reflected and transmitted beams. Because no critical slope occurs for $s$=±0.005, beams originate where the topographic slope is closest to the internal-wave propagation angle (i.e., the steepest slope). In other cases, beams originate from critical slopes or the trough of a canyon-like forbidden zone (e.g., for $s$=±0.01 and $H_g$=1000 m, shown in Fig. 7).

In general, reflection ensures continuous velocity and density (or pressure) where wave speed, horizontal wavenumbers, or vertical modal structures change (or pressure, Kelly et al. 2013). Normal modes can be calculated in buoyancy coordinates using (26), allowing us to compare eigenspeed variations with and without a horizontal buoyancy gradient. When there is no horizontal buoyancy gradient, the surface and bottom topography in Cartesian coordinates are

$$\eta = sW \tag{40}$$

and

$$h = -H + sW\left[\beta - (1-\beta)\tanh\frac{x}{W}\right]. \tag{41}$$

Thus, the topography and horizontal buoyancy gradients produce identical boundaries when viewed in buoyancy coordinates. E.g., if $s$=±0.005, mode-one eigenspeeds vary across the geostrophic front and bottom topography (Fig. 10a and 10b). For the topography given by (41), horizontal variation of speed is larger with a horizontal buoyancy gradient than without, implying that a geostrophic front impedes internal-wave propagation. The joint effects of topography and horizontal buoyancy gradients on reflection coefficients (Fig. 10c for $s$=±0.005 and Fig. 10d for $s$=±0.01) differ from the isolated effects of a horizontal buoyancy gradient (Fig. 10e and 10f). Thus, a geostrophic front enhances interactions between internal waves and topography. E.g., reflection is nearly zero if the bottom boundary is flat and there is no front [$\beta$=1 in (41), note that trivial reflection arises from a sloping boundary defined by (40)], but reflection always occurs when there is a front because eigenspeeds vary across the front. Scattering is only avoided in a special case where the stratification and topography are both linear functions of $x$ and parallel to each other. Normal-mode analysis is not applicable when $s$=±0.01 because a forbidden zone does not permit wave solutions.

Overall, the idealized results here indicate that internal-wave scattering at a shelf break is greatly increased by the presence of a shelf-break front. These dynamics may affect global estimates of slope reflectivity (Hall et al. 2013; Klymak et al. 2016) because fronts are commonly observed on continental shelves (Flagg and Beardsley 1978; Houghton et al. 1988), and can be surface intensified (Flagg et al. 2006), bottom intensified (Walker et al. 2013), or vertically unidirectional (Barth et al. 2004).

## 4. Ray Propagation and Wave Tunneling

Internal-wave rays emanate from critical slopes on topographic features. These rays may subsequently encounter a geostrophic front associated with a boundary current, e.g., the Kuroshio in Luzon Strait. Here we examine an idealized ray

$$\varphi = -iA\exp\left[ (\frac{z - z_0}{\delta})^2 \right], \tag{42}$$

propagating into the domain from the left boundary and crossing a geostrophic front. Here, $z_0$ indicates the initial location of the ray and $\delta$ its width. With this definition, two rays are generated: one propagating upwards and the other downwards.

For a weak front with no forbidden zone, the ray path bends as it propagates through the front, but energy is transmitted. If a forbidden zone is present, strong reflection from the virtual boundary $\Delta$=0 occurs (Fig. 11), and a reflected ray propagates along a characteristic. Wave solutions are not allowed in the forbidden zone, but an attenuated ray penetrates the forbidden zone due to wave tunneling (Bender and Orszag 1978). This attenuated ray extends to the lee side of the forbidden zone and continues to propagate rightwards when it emerges in an area with $\Delta$>0. Tunneling effects were also examined by Sutherland and Yewchuk (2004), but tunneling at a front has not been observed in the ocean.

## 5. Application in Luzon Strait

Luzon Strait is a site of energetic internal-tide generation. The Kuroshio flows through the region forming westward shoaling stratification in geostrophic balance (Fig. 12). A meandering Kuroshio can modulate internal-tide generation and scattering at the two ridges in Luzon Strait (Fig. 1a). The eastern Lan-Yu Ridge generates stronger internal tides than the western Heng-

Chun Ridge because it is shallower, but the Heng-Chun Ridge also plays a significant role in internal-tide generation. Depending on the phase of the internal tides arriving from Lan-Yu Ridge, local internal tide generation by Heng-Chun Ridge may be enhanced or reduced (Li et al. 2016), modulating internal tides propagating into the South China Sea. These propagating internal tides may break in the deep basin and produce large-amplitude internal solitary waves (Farmer et al. 2009). Heng-Chun Ridge can also reflect westward-propagating internal tides generated at Lan-Yu Ridge and scatters them to high modes that fuel local mixing (Buijsman et al. 2012). In this section, the latter effect will be examine in the presence of a horizontal buoyancy gradient associated with Kuroshio.

Observed background stratification is approximated by analytical functions

$$N^2 = N_0^2(z) + \frac{\sqrt{\pi}}{2} fV_0 \frac{W}{D} \operatorname{erf}\left(\frac{x-x_1}{W}\right) \cdot \exp\left(\frac{z}{D}\right) \tag{43}$$

and

$$M^2 = \frac{f}{D} \exp\left[-\frac{(x-x_1)^2}{W^2}\right] \cdot \exp\left(\frac{z}{D}\right) \tag{44}$$

to avoid numerical instability. The corresponding geostrophic velocity is

$$V = V_0 \exp\left(-\frac{(x-x_1)^2}{W^2}\right) \cdot \left[\exp\left(\frac{z}{D}\right) - \exp\left(-\frac{H_g}{D}\right)\right]. \tag{45}$$

Here, $V_0$ represents the maximum geostrophic velocity, and $x_1$, $D$ and $W$ the center, depth and width of the front. $N_0^2$ is fitted using a 15-order polynomial function to averaged buoyancy frequency profile (Fig. 12d) acquired from the CTD casts conducted during two cruises in 2005 and 2007 in the Nonlinear Internal Wave Initiative experiment (Farmer et al. 2009). Locations of the CTD casts are scattered, and we do not have direct stratification measurements across Luzon Strait. However, we can compare our inferred profiles with the reanalysis dataset from a global HYCOM simulation. We choose $V(H_g)$ = 0 m s$^{-1}$, $H_g$ = 3500 m, $D$ = 300 m and $W$ = 50 km to obtain the horizontal distribution of background stratification and geostrophic flow (Fig. 12e), in agreement with the HYCOM data (Fig. 12b). The bottom topography is a Gaussian function centered at $x_0$

$$h = -H_0 + h_r \exp\left[-\frac{\left(x - x_0\right)^2}{W_r^2}\right], \tag{46}$$

for Heng-Chun Ridge with total depth $H_0$ = 3500 m, ridge height $h_r$ = 1800 m and width $W_r$ = 20 km (see the schematic of wave propagation in Fig. 13a).

Both Heng-Chun Ridge and the Kuroshio reflect the westward-propagating internal waves generated at Lan-Yu Ridge. For realistic stratification (43), reflection by the bottom boundary is much greater than by the horizontal buoyancy gradient $M^2$, because if the topography were eliminated, there would be no critical slope or forbidden zone due to the horizontal buoyancy gradient alone. If both topography and a horizontal buoyancy gradient are present, total reflectivity depends on the separation of the ridge and front. A higher ratio of the surface buoyancy slope to the internal wave characteristic produces a more reflective front; therefore, reflection is more significant for $K_1$ internal waves than $M_2$. In addition, interactions between the $M_2$ internal wave ray and sloping surface boundary makes the $M_2$ analysis complicated than $K_1$. Here, we only examine reflection coefficients for $K_1$ internal waves. Standing waves form between the ridge and front if their separation distance is a multiple of the half the mode-$j$ wavelength, $0.5\lambda_j$. Therefore, mode-one reflection varies sinusoidally with separation distance over half a mode-one wavelength (Fig. 13a). Reflected or transmitted energy in higher modes varies analogously according to each mode's wavelength.

An idealized model can explain the above sensitivity. As illustrated in Fig. 13b, the domain has two regions with dissimilar stratification that meet at $x_1$. The stratification in each region is given by (43) as $\Delta x=(x_1-x_0)\rightarrow\pm\infty$. Bottom topography is represented by a top-hat ridge with the same height $h_r$ and width $W_r$ in (46) also centered at $x_0$. This model is solved numerically by matching horizontal velocity and pressure at the interfaces with discontinuous stratification and bottom topography (Kelly et al. 2013). Mode-one reflectivity for $K_1$ internal waves incident from the east boundary depends on the separation between the ridge and front (Figs. 14b). If the front is on the left side of the ridge ($\Delta x>0$), the mode-one reflection coefficient reaches a minimum when their separation is an integer multiple of half wavelength of mode-one internal waves. If the front is on the right ($\Delta x<0$), reflection reaches a maximum. The exact magnitude and phase of the reflection coefficients in the idealized model differs from the solutions to (12) because the ridge and front shapes have been simplified.

## 6. Summary and Discussion

Reflection and scattering occur where internal waves propagate across horizontally varying topography or stratification. In most regions, horizontal buoyancy gradients are weak (Fig. 1b), so topographic effects dominate. However, in regions with strong geostrophic fronts, such as the Kuroshio or Gulf Stream, horizontal buoyancy gradients and shear cannot be ignored.

2D internal wave propagation across a geostrophic front depends on the absolute geostrophic velocity (not just shear), isopycnal slope, topographic slope and incident wave mode. It is difficult to state the effects of these parameters in any unique region, but realistic solutions can be rapidly obtained by numerically solving the modified internal wave equation (12), where $\Delta$ defined in (14) determines the type of PDE. In buoyancy coordinates, (12) appears as a canonical PDE in conventional internal wave theory (Turner 1973), but with a new critical condition when the boundary slope is parallel to the wave characteristics. In this reference frame, horizontal buoyancy gradients produce effects analogous to bottom topography, providing a new way to interpret internal-wave propagation through a geostrophic front. That is, previous studies of internal-tide-topography interactions (e.g., Chapman and Hendershott 1981, Klymak et al 2013, Kelly et al 2013) now help explain how low-mode internal waves are scattered by horizontal buoyancy gradients, even where the bottom is flat in Cartesian coordinates. The equations in buoyancy coordinates also show that a western boundary current, like the Kuroshio, can interact with distant ridges to produce resonances similar to a double-ridge system (Li 2014).

Solutions to (12) are sensitive to regions of negative $\Delta$ (i.e., forbidden zones), which act like a barrier, blocking internal wave propagation and causing reflection. Strong scattering appears around $\Delta$=0 or at critical points on the boundaries.

Low-mode internal waves can scatter from tilted isopycnals to produce high-mode waves. Wave-wave interactions and other nonlinear processes (McComas and Bretherton 1977; McComas and Muller 1981; reviewed by Sarkar and Scotti 2016) can dissipate high-mode waves and contribute to diapycnal mixing (St. Laurent et al. 2011; van Haren and Gostiaux 2012; Klymak et al. 2013; Hennon et al. 2014) that affects the overturning circulation (Nikurashin and Ferrari 2013; Wagner and Young 2016; Kunze 2017b). Strong interactions between fronts and internal waves can even drive energy loss from both features (Thomas 2017). Thus, internal wave scattering at geostrophic fronts may provide a pathway to energy dissipation in the global ocean.

We estimate a dissipation rate from solutions to (12) using the recipe introduced by Klymak et al. (2013), which quantifies energy flux into locally trapped high-mode internal waves in terms of the least mode number $\kappa$ such that the Froude number

$$Fr = \frac{U_\kappa}{c_\kappa} \geq 1, \tag{47}$$

where $U_\kappa$ is the maximum horizontal velocity attributable to the first $\kappa$ modes

$$U_\kappa = \max\left[\sum_{m=1}^{\kappa} u_m(x,z)\right]. \tag{48}$$

Wave modes $m<\kappa$ escape from the front, but higher modes are trapped and dissipate locally. Hence the total across-front dissipation $D$ is the vertically-integrated energy flux in reflected and transmitted waves with mode-number $m>\kappa$

$$D = \int_{-H}^{0} \left( -\sum_{m=\kappa^r}^{\infty} J_m^r + \sum_{m=\kappa^t}^{\infty} J_m^t \right) dz. \quad \text{[unit: W m}^{-1}\text{]} \tag{49}$$

Here, $J_m$ is the energy flux of mode-$m$ internal waves and the superscripts $r$ and $t$ represent reflected and transmitted waves, respectively. The cutoff mode number $\kappa$ may be different for reflected and transmitted waves, implying that the dissipation is asymmetric on each side of the front. We computed $D$ for isopycnal slopes $s$ = ±0.01 (Fig. 15) using the model configuration in section 3.2. The bottom is flat ($H$=2000 m), so high modes only arise by scattering at the front. The cutoff mode number decreases as the incident wave amplitude increases (from $U_0$ = 0.1 – 1 m s$^{-1}$), causing $D$ to increases from $10^{-2}$ – $10^{3}$ W m$^{-1}$. This corresponds to an average dissipation rate of $10^{-13}$ to $10^{-8}$ W kg$^{-1}$ if we divide $D$ by reference density (1000 kg m$^{-3}$), the depth of the front (2000 m), and the width of the front (50 km). This rate is smaller than the dissipation rate in

Luzon Strait ($10^{-8}$ – $10^{-6}$ W $kg^{-1}$; Yang et al. 2016; Alford et al. 2011), but comparable to the background dissipation rate in ocean ($10^{-9}$ W $kg^{-1}$; Waterhouse et al. 2014; Kunze et al. 2017a). High resolution numerical models and/or in situ observations are needed to validate our estimates and determine the importance of feedbacks between internal–wave driven mixing and geostrophic flows.

**Acknowledgement**

We thank two anonymous reviewers for their helpful comments. QL is supported by NSFC-41576008, LTO1503, QNHX1602. XM is supported by the National Basic Research Program of China (973 Program, 2014CB745002). SC is supported by NSFC-41430964, Key Research Program of Frontier Sciences, CAS(QYZDJ-SSW-DQC034). Numerical computation is supported by Special Program for Applied Research on Super Computation of the NSFC-Guangdong Joint Fund under Grant No. U1501501.

## References


Alford, M.H., J.A. MacKinnon, J.D. Nash, H. Simmons, A. Pickering, J.M. Klymak, R. Pinkel, O. Sun, L. Rainville, R. Musgrave, T. Beitzel, K. Fu, and C. Lu, 2011: Energy Flux and Dissipation in Luzon Strait: Two Tales of Two Ridges. J. Phys. Oceanogr., 41, 2211–2222.

Balmforth, N.J. and T. Peacock, 2009: Tidal Conversion by Supercritical Topography. J. Phys. Oceanogr., 39, 1965–1974.

Barth, J.A., D. Hebert, A.C. Dale, and D.S. Ullman, 2004: Direct Observations of Along-Isopycnal Upwelling and Diapycnal Velocity at a Shelfbreak Front. J. Phys. Oceanogr., 34, 543–565.

Bender C. M. and S. A. Orszag 1978: Advanced Mathematical Methods for Scientists and Engineers I, Springer, 593pp.

Bishop, S.P., D.R. Watts, J. Park, and N.G. Hogg, 2012: Evidence of Bottom-Trapped Currents in the Kuroshio Extension Region. J. Phys. Oceanogr., 42, 321–328.

Buijsman, M. C., J. C. McWillianms, and C. R. Jackson, 2010: East-west asymmetry in nonlinear internal waves from Luzon Strait, J. Geophys. Res., 115, C10057, doi:10.1029/2009JC006004.

Buijsman, M.C., S. Legg, and J. Klymak, 2012: Double-Ridge Internal Tide Interference and Its Effect on Dissipation in Luzon Strait. J. Phys. Oceanogr., 42, 1337–1356.

Chapman D. C. and M. C. Hendershott, 1981: Scattering of internal waves obliquely incident upon a step change in bottom relief, Deep Sea Research Part A., 28(11), 1323-1338.

Chu, P. C., Li, R. F., 2000. South China Sea isopycnal surface circulations.J. Phys. Oceanogr. 30: 2419–2438.

Chuang, W., and D. Wang, 1981: Effects of density front on the generation and propagation of internal tides. J. Phys. Oceanogr., 11, 1357–1374.

Damerell, G. M., K. J. Heywood, and D. P. Stevens, 2013: Direct observations of the Antarctic circumpolar current transport on the northern flank of the Kerguelen Plateau, J. Geophys. Res. Oceans, 118, 1333–1348.

Duda, T. F., Y. Lin, M. Buijsman, and A. E. Newhall, 2018: Internal Tidal Modal Ray Refraction and Energy Ducting in Baroclinic Gulf Stream Currents. J. Phys. Oceanogr., 48, 1969–1993.

Dunphy, M., and K. G. Lamb, 2014: Focusing and vertical mode scattering of the first mode internal tide by mesoscale eddy interaction, J. Geophys. Res., 119, 523–536, doi:10.1002/2013JC009293.

Farmer, D.M., 1978: Observations of Long Nonlinear Internal Waves in a Lake. J. Phys. Oceanogr., 8, 63–73.

Farmer, D. M., Q. Li and J. Park 2009: Internal wave observations in the South China Sea: The role of rotation and non‐linearity, Atmosphere-Ocean, 47:4, 267-280.

Flagg, C. N., and R. C. Beardsley, 1978: On the stability of the shelf water/slope water front south of New England, J. Geophys. Res., 83(C9), 4623–4631.

Flagg, C. N., M. Dunn, D.‐P. Wang, H. T. Rossby, and R. L. Benway, 2006: A study of the currents of the outer shelf and upper slope from a decade of shipboard ADCP observations in the Middle Atlantic Bight, J. Geophys. Res., 111, C06003.

Gill 1982: Atmosphere-Ocean Dynamics, Academic Press, 662pp.

Hall, R.A., J.M. Huthnance, and R.G. Williams, 2013: Internal Wave Reflection on Shelf Slopes with Depth-Varying Stratification. J. Phys. Oceanogr., 43, 248–258.

van Haren, H., and L. Gostiaux, 2012: Energy release through internal wave breaking, Oceanography, 25(2),124–131.

Hennon, T. D., S. C. Riser, and M. H. Alford, 2014: Observations of internal gravity waves by Argo floats. J. Phys. Oceanogr., 44, 2370–2386.

Houghton, R. W., F. Aikman III, and H. W. Ou, 1988: Shelf-slope frontal structure and cross-shelf exchange at the New England shelf-break. Cont. Shelf Res., 8(5–7), 687–710.

Kaneko, H., I. Yasuda, K. Komatsu, and S. Itoh, 2012: Observations of the structure of turbulent mixing across the Kuroshio, Geophys. Res. Lett., 39, L15602.

Kelly, S. M., N. L. Jones, and J. D. Nash, 2013: A Coupled Model for Laplace's Tidal Equations in a Fluid with One Horizontal Dimension and Variable Depth. J. Phys. Oceanogr., 43, 1780–1797.

Kelly, S. M. and P. F. J. Lermusiaux, 2016: Internal‐tide interactions with the Gulf Stream and Middle Atlantic Bight shelfbreak front, J. Geophys. Res. Oceans, 121, 6271–6294.

Klein P., H. Bach-Lien, C. Xavier, 2003: Emergence of cyclonic structures due to the interaction between near-inertial oscillations and mesoscale eddies . Quarterly Journal Of The Royal Meteorological Society, 129(593), 2513-2525.

Klymak, J.M., M. Buijsman, S. Legg, and R. Pinkel, 2013: Parameterizing Surface and Internal Tide Scattering and Breaking on Supercritical Topography: The One- and Two-Ridge Cases. J. Phys. Oceanogr., 43, 1380–1397.

Klymak, J.M., H.L. Simmons, D. Braznikov, S. Kelly, J.A. MacKinnon, M.H. Alford, R. Pinkel, and J.D. Nash, 2016: Reflection of Linear Internal Tides from Realistic Topography: The Tasman Continental Slope. J. Phys. Oceanogr., 46, 3321–3337.

Kunze, E. and T. Sanford, 1984: Observations of near-inertial waves in a front. J. Phys. Oceanogr., 14, 566–581.

Kunze, E., 1985: Near-inertial wave propagation in geostrophic shear. J. Phys. Oceanogr., 15, 544–565.

Kunze, E., 1986: The Mean and Near-Inertial Velocity Fields in a Warm-Core Ring. J. Phys. Oceanogr., 16, 1444–1461.

Kunze, E., R. W. Schmitt, and J. M. Toole, 1995: The Energy Balance in a Warm-Core Ring's Near-Inertial Critical Layer. J. Phys. Oceanogr., 25, 942–957.

Kunze, E., 2017a: Internal-Wave-Driven Mixing: Global Geography and Budgets. J. Phys. Oceanogr., 47, 1325–1345.

Kunze, E., 2017b: The Internal-Wave-Driven Meridional Overturning Circulation. J. Phys. Oceanogr., 47, 2673–2689.

Lamb, K.G. and J.A. Shore, 1992: The Influence of Horizontal Inhomogeneities on the Propagation of High-Frequency Linear Internal Gravity Waves across a Baroclinic Flow. J. Phys. Oceanogr., 22, 965–975.

St. Laurent, L., Simmons, H., Tang, T., & Wang, Y. (2011). Turbulent Properties of Internal Waves in the South China Sea. Oceanography, 24(4), 78-87.

Li, Q., 2014: Numerical assessment of factors affecting nonlinear internal waves in the South China Sea, Prog. Oceanogr., 121, 24–43.

Li, Q., B. Wang, X. Chen, X. Chen, and J.-H. Park, 2016: Variability of nonlinear internal waves in the South China Sea affected by the Kuroshio and mesoscale eddies, J. Geophys. Res. Oceans, 121, 2098–2118, doi:10.1002/2015JC011134.

Lighthill, M. J. 1978 Waves in Fluids. Cambridge University Press, 504 pp.

Lindzen R. S. and H. L. Kuo, 1969: A reliable method for the numerical integration of a large class of ordinary and partial differential equations. Mon. Wea. Rev., 97, 732-734.

Locarnini, R. A., Mishonov, A. V., Antonov, J. I., Boyer, T. P., Garcia, H. E., 2006. In: Levitus, S. (Ed.), World Ocean Atlas 2005. Temperature, vol. 1. NOAA Atlas NESDIS 61, U.S. Gov. Printing Office, Washington, DC, 182 pp.

Lueck, R. G. and T. R. Osborn, 1986: The dissipation of kinetic energy in a warm‐core ring, J. Geophys. Res., 91(C1), 803‐818.

Magaard, L., 1968: Ein Beitrag zur Theorie der internen Wellen als Stoerungen geostrophischer Stroemungen (A contribution to the theory of internal waves as perturbations of geostrophic currents). Dt. hydrogr. Z., 21, 241–278.

Marshall, J., Adcroft, A., Hill, C., Perelman, L., Heisey, C., 1997: A finite volume, incompressible Navier-Stokes model for studies of the ocean on parallel computers. Journal of Geophysical Research 102, 5753–5766.

Martini, K.I., M.H. Alford, E. Kunze, S.M. Kelly, and J.D. Nash, 2011: Observations of Internal Tides on the Oregon Continental Slope. J. Phys. Oceanogr., 41, 1772–1794.

McComas, C. H., and F. P. Bretherton, 1977: Resonant interaction of oceanic internal waves, J. Geophys. Res., 82(9), 1397–1412.

McComas, C.H. and P. Müller, 1981: Time Scales of Resonant Interactions Among Oceanic Internal Waves. J. Phys. Oceanogr., 11, 139–147.

Meyer, A., B. M. Sloyan, K. L. Polzin, H. E. Phillips, and N. L. Bindoff, 2015: Mixing Variability in the Southern Ocean. J. Phys. Oceanogr., 45, 966–987.

Mooers, C. N. K., 1975: Several effects of a baroclinic current on the crossstream propagation of inertial-internal waves. Geophys. Fluid Dyn., 6, 245–275.

Nagai, T., A. Tandon, E. Kunze, and A. Mahadevan, 2015: Spontaneous Generation of Near-Inertial Waves by the Kuroshio Front. J. Phys. Oceanogr., 45, 2381–2406.Nash, J.D., S.M. Kelly, E.L. Shroyer, J.N. Moum, and T.F. Duda, 2012: The Unpredictable Nature of Internal Tides on Continental Shelves. J. Phys. Oceanogr., 42, 1981–2000.

Nash, J.D., S.M. Kelly, E.L. Shroyer, J.N. Moum, and T.F. Duda, 2012: The Unpredictable Nature of Internal Tides on Continental Shelves. J. Phys. Oceanogr., 42, 1981–2000.

Nikurashin, M., and R. Ferrari, 2013: Overturning circulation driven by breaking internal waves in the deep ocean, Geophys. Res. Lett., 40, 3133–3137, doi: 10.1002/grl.50542.

Olbers, D.J., 1981: The Propagation of Internal Waves in a Geostrophic Current. J. Phys. Oceanogr., 11, 1224–1233.

Os

Osborne, J.J., A.L. Kurapov, G.D. Egbert, and P.M. Kosro, 2011: Spatial and Temporal Variability of the M2 Internal Tide Generation and Propagation on the Oregon Shelf. J. Phys. Oceanogr., 41, 2037–2062.

Peters, H., 1983: The Kinematics of a Stochastic Field of Internal Waves Modified by a Mean Shear Current, Deep-Sea Research, 30, 119–148.

Pétrélis, F., S.L. Smith, and W.R. Young, 2006: Tidal Conversion at a Submarine Ridge. J. Phys. Oceanogr., 36, 1053–1071.

Rainville, L., and R. Pinkel, 2004: Observations of energetic highwavenumber internal waves in the Kuroshio. J. Phys. Oceanogr., 34, 1495–1505.

— and —, 2006: Propagation of Low-Mode Internal Waves Through the Ocean. J. Phys. Oceanogr., 36, 1220-1236.

Robinson, R. M., 1969: The effects of a barrier on internal waves. Deep Sea Research 16, 421–429.

Sarkar S. and A. Scotti, 2017: From Topographic Internal Gravity Waves to Turbulence, Annual Review of Fluid Mechanics, 49, 195-220.

Stommel, H. and F. Schott, 1977: The beta spiral and the determination of the absolute velocity field from hydrographic station data, Deep Sea Res., 24, 325-329.

Sutherland, B. and K. Yewchuk, 2004: Internal wave tunnelling. J. Fluid Mech., 511, 125-134. doi:10.1017/S0022112004009863.

Thomas, L. N., J. R. Taylor, E. A. D'Asaro, C. M. Lee, J. M. Klymak and A. Y. Shcherbina, 2016: Symmetric instability, inertial oscillations, and turbulence at the Gulf Stream front, J. Phys. Ocean., 46, 197-217.

Thomas, L. N., 2017: On the modifications of near-inertial waves at fronts: implications for energy transfer across scales, Ocean Dynamics, 67(10), 1335-1350.

Turner, J., 1973: Buoyancy Effects in Fluids (Cambridge Monographs on Mechanics). Cambridge: Cambridge University Press, 368pp.

Wagner, G. L and W. R. Young, 2016: A three-component model for the coupled evolution of near-inertial waves, quasi-geostrophic flow and the near-inertial second harmonic, J. Fluid Mech., 802, 806-837.

Walker, D. P., A. Jenkins, K. M. Assmann, D. R. Shoosmith, and M. A. Brandon, 2013: Oceanographic observations at the shelf break of the Amundsen Sea, Antarctica, J. Geophys. Res. Oceans, 118, 2906–2918.

Waterhouse, A.F., J.A. MacKinnon, J.D. Nash, M.H. Alford, E. Kunze, H.L. Simmons, K.L. Polzin, L.C. St. Laurent, O.M. Sun, R. Pinkel, L.D. Talley, C.B. Whalen, T.N. Huussen, G.S. Carter, I. Fer, S. Waterman, A.C. Naveira Garabato, T.B. Sanford, and C.M. Lee, 2014: Global Patterns of Diapycnal Mixing from Measurements of the Turbulent Dissipation Rate. J. Phys. Oceanogr., 44, 1854–1872.

Whalen, C. B., L. D. Talley, and J. A. Mackinnon, 2012: Spatial and temporal variability of global ocean mixing inferred from Argo profiles. Geophys. Res. Lett., 39, L18612, doi:10.1029/2012GL053196.

Whitt, D. B., and L. N. Thomas, 2013. Near-inertial waves in strongly baroclinic currents, J. Phys. Oceanogr., 43, 706-725.

Wunsch, C., 1978: The general circulation of the North Atlantic west of 50°W determined from inverse method. Rev. Geophys., 16, 583–620.

Yang, Q., W. Zhao, X. Liang, and J. Tian, 2016: Three-Dimensional Distribution of Turbulent Mixing in the South China Sea. J. Phys. Oceanogr., 46, 769–788.

Young, W.R. and M. Ben-Jelloul, 1997. Propagation of near-inertial oscillations through a geostrophic flow. J. Mar. Res., 55, 735-766.

Zaron, E. D. and G. D. Egbert, 2014: Time‐variable refraction of the internal tide at the Hawaiian Ridge, J. Phys. Oceanogr., 44, 538–557.

**TABLE 1**

**Parameters in the MITgcm**

| Parameters | Notation | Value |
|---|---|---|
| Horizontal eddy viscosity coefficient | $A_h$ | $1.0\times10^{-5}$ m$^2$ s$^{-1}$ |
| Vertical eddy viscosity coefficient | $A_v$ | $1.0\times10^{-5}$ m$^2$ s$^{-1}$ |
| Horizontal diffusion coefficient | $K_h$ | 0 m$^2$ s$^{-1}$ |
| Vertical diffusion coefficient | $K_v$ | 0 m$^2$ s$^{-1}$ |
| Horizontal grid size | $\Delta x$ | 493 m |
| Vertical grid size | $\Delta z$ | 10 m |
| Time step | $\Delta t$ | 2.5 s |
| Gravitational acceleration | $g$ | 9.8 m s$^{-2}$ |
| Domain width | $L$ | 4038 km |
| Domain depth | $H$ | 2000 m |
| Reference salinity | $S_r$ | 35 psu |

## Figure Captions

**Figure 1:** Global distribution of maximum isopycnal slope |*S*| in the upper 100-1000 m, calculated using the climatological temperature and salinity from World Ocean Atlas (Locarnini et al. 2006, spatial resolution: 0.25°×0.25°). Isopycnal slope *S* changes with depth and also depends on the scale on which gradients are calculated (i.e., 0.25°×0.25° here). Only maximum |*S*| are shown in logarithmic scale. Stratification in the upper 100 m is not used in order to avoid extraordinarily large values in the mixed layer where the buoyancy frequency $N^2$ is nearly zero.

**Figure 2:** Snapshots of (a) the analytic solution of (12) and (b) the numerical simulation using the MITgcm for rightward-propagating mode-one internal waves with $M_2$ tidal frequency incident on a front at $x$=0. The difference between (a) and (b) is shown in (c). In both cases, the isopycnal slope $s=-0.1$, thermal-wind reference level $H_g$ = 1000 m, vertical buoyancy frequency $N = 5\times10^{-3}$ s$^{-1}$ and front width $W$ = 25 km. Configuration of the MITgcm is given in Table 1. White contours are isopycnals at 1 kg m$^{-3}$ intervals; normalized instantaneous velocity $u$ of internal waves is in red and blue colors. Black contours in (b) are isopycnals disturbed by internal waves.

**Figure 3:** Rightward mode-one internal waves incident on a front at $x$=0. The total (top), reflected (middle) and transmitted (bottom) wave fields are plotted in the $z$ (left) and buoyancy $B$ (right) coordinates, respectively. Parameters of the internal waves and front are the same as Fig. 2a.

**Figure 4:** (a) Reflection and transmission coefficients for different selection of reference level $H_g$ in the thermal wind calculation. (b) The energy flux ratio between the reflected and transmitted mode 1 waves and the incident waves. (a) and (b) are similar because most reflection and transmission are in mode-one. (c) The energy flux ratio between the reflected and transmitted high-mode waves and the incident waves. Black for the reflected waves and gray for transmitted. $J_i$ represents the energy flux of incident waves. $J_r$ represents the energy flux of reflected or transmitted waves when the internal waves propagate across a geostrophic front. $J_{r1}$ is the energy flux for the mode-one waves. I, II and III indicate regimes defined in section 3.1. In this figure, front parameters $s = -0.01$, $N = 5\times10^{-3}$ $s^{-1}$ and $W = 25$ km.

**Figure 5:** Wave fields (color) in buoyancy coordinates for $M_2$ internal waves propagating across a geostrophic front. Top, middle and bottom panels show total, reflected and transmitted wave fields, respectively. Left, middle and right panels represent thermal-wind reference levels $H_g$=0 m, 1000 m and 2000 m, respectively. Black dashed lines show the ray paths. Black solid contours highlight $\Delta$=0. Black dash-dot contours are the geostrophic flow $V$ with 0.5 m s-1 intervals and green solid curves indicate the reference level where $V$=0. Black crosses indicate the critical points on the bottom or surface boundaries. In this figure, $s = -0.01$, $N = 5\times10^{-3}$ $s^{-1}$ and $W = 25$ km.

**Figure 6:** Energy flux ratio of reflected (black) and transmitted waves (gray) to the incident waves, as a function of isopycnal slopes $s$, for (a) total, (b) mode 1, (c) mode 2 and (d) high-

mode waves. In this figure, the other front parameters $H_g$ = 2000 m, $N$ = 5×10$^{-3}$ s$^{-1}$ and $W$ = 25 km.

**Figure 7:** Wave fields for isopycnal slope $s$=-0.01 (left) and $s$=0.01 (right). Solid black contours highlight $\Delta$=0. Black crosses indicate the critical points on the surface boundary. The front parameters are the same as Fig. 6.

**Figure 8:** (a) shows reflection coefficients as a function of mode numbers for different isopycnal slopes $s$=±0.005 and ±0.01 with $M_2$ tidal frequency. (b), (c) and (d) show the total, reflected and transmitted wave fields for the incident mode-8 $M_2$ internal waves, respectively. Bold black curves indicate the virtual boundary $\Delta$=0 and black crosses the critical slopes. Other front parameters $H_g$ = 2000 m, $N$ = 5×10$^{-3}$ s$^{-1}$ and $W$ = 25 km.

**Figure 9:** Wave fields for different topographic slope $\beta$ and isopycnal slope $s$ in Cartesian (the 1st and 3rd rows) and buoyancy coordinates (the 2nd and 4th rows). Density is only shown in the Cartesian coordinates as black contours and ignored in the buoyancy coordinates. Red and blue colors indicate the normalized horizontal velocity $u$ of internal waves. Other front parameters $H_g$ = 2000 m, $N$ = 5×10$^{-3}$ s$^{-1}$ and $W$ = 25 km.

**Figure 10:** (a) and (b) show phase speed of mode-one $M_2$ internal waves across the front for isopycnal slopes $s$=±0.005, respectively. The bottom topography is defined in formula (38). $\beta$ is

the ratio of bottom to isopycnal slope. (c) and (d) are reflection coefficients $J_r/J_i$ as a function of $\beta$ for $s$=±0.005 and $s$=±0.01. In (e) and (f), although horizontally uniform stratification is assumed, reflection coefficients are computed using the same bottom topography as in (c) and (d). Front parameters are the same as Fig. 9.

**Figure 11:** Wave field $u/U_0$ for an internal-wave beam propagating across a geostrophic front in the buoyancy coordinates. The incident ray originates from the black triangle on the west boundary. Bold black curves indicate the virtual boundary $\Delta$=0 and black crosses the critical slopes. Three dashed lines are superimposed on the wave field to highlight ray propagation. The green and black rays propagate across the front, but the gray one reflects from the virtual boundary. Front parameters are $s = -0.01$, $H_g$ = 2000 m, $N = 5\times10^{-3}$ s$^{-1}$ and $W$ = 25 km.

**Figure 12:** (a) Temperature at 500 m depth (color) and current velocity at surface on 5 August 2007 in the HYCOM model. (b) Temperature (white contours) superimposed on meridional velocity (color, m s$^{-1}$) for the upper 1000 m from HYCOM. Bottom topography averaged between 20°N and 21°N is shaded in gray. (c) and (d) show density and buoyancy frequency squared profiles, in which the red curves are averaged from CTD casts and the blue ones approximated using polynomial curve fitting. (e) Fitted temperature (contours) and meridional velocity (color, m s$^{-1}$) using (43) and (44).

**Figure 13:** Schematics for models applied in Luzon Strait. Incident waves come from the east. The top is for (12) and the bottom is for the simplified model. Arrows in the bottom panel

indicate directions of wave propagation. $x_0$ and $x_1$ indicate the locations of the ridge and front, respectively.

**Figure 14:** Reflection coefficients for $K_1$ mode-one internal tides propagating across Heng-Chun Ridge computed using (12) (a) and using the simplified model (b). $\Delta x = x_1 - x_0$ is the separation between the front and ridge shown in Fig. 13b. Data in (b) for $\Delta x \leq 10$ km are missing due to overlap between the ridge and interface between two stratifications, which cannot be resolved by the simplified model.

**Figure 15:** (a) Cutoff mode numbers $\kappa$ and (b) dissipation for different amplitude $U_0$ of incident mode-one $M_2$ internal waves with isopycnal slopes $s=\pm0.01$.

## Figures

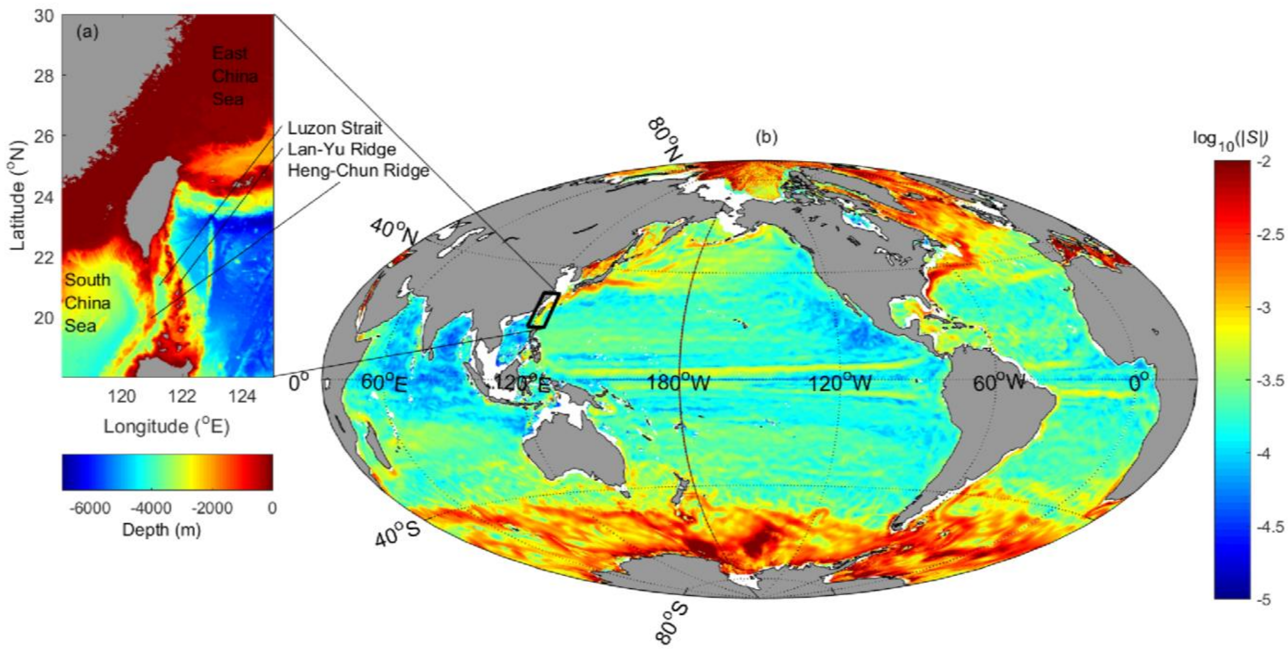


**Figure 1:** (a) Geographical locations and bathymetry of the East and South China Sea. (b) Global distribution of maximum isopycnal slope $|S|$ in the upper 100-1000 m, calculated using the climatological temperature and salinity from World Ocean Atlas (Locarnini et al. 2006, spatial resolution: 0.25°×0.25°). Isopycnal slope $S$ changes with depth and is sensitive to the scale on which gradients are calculated. Only maximum $|S|$ are shown in logarithmic scale. Stratification in the upper 100 m is not used to avoid extremely large values in the mixed layer where the buoyancy frequency $N^2$ is nearly zero.

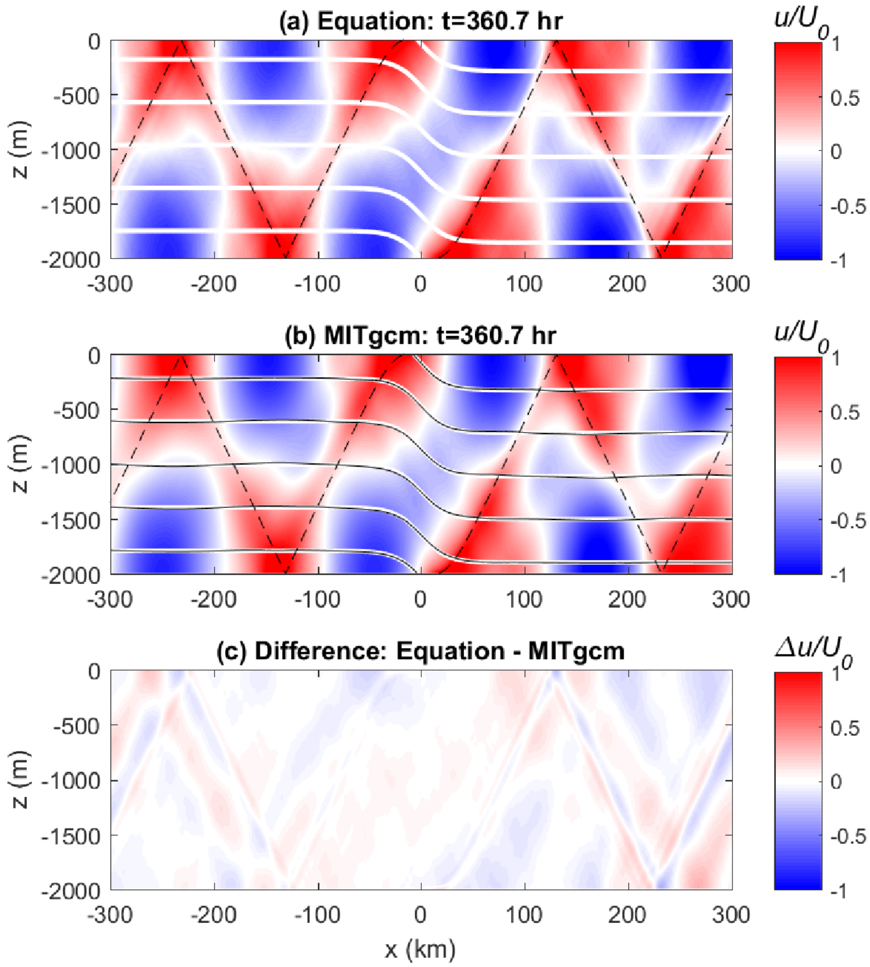


**Figure 2:** Snapshots of (a) an analytic solution of (12) and (b) the numerical simulation using the MITgcm for rightward-propagating mode-one internal waves with $M_2$ tidal frequency incident on a front at $x$=0. The difference between (a) and (b) is shown in (c). In both cases, the maximum isopycnal slope $s = -0.01$, level of no motion $H_g$ = 1000 m, vertical buoyancy frequency $N$ = $5\times10^{-3}$ $s^{-1}$ and front width $W$ = 25 km. The configuration for the MITgcm is given in Table 1. White contours are isopycnals at 1 kg $m^{-3}$ intervals; normalized instantaneous velocity $u$ of internal waves is in red and blue. Black contours in (b) are isopycnals disturbed by internal waves.

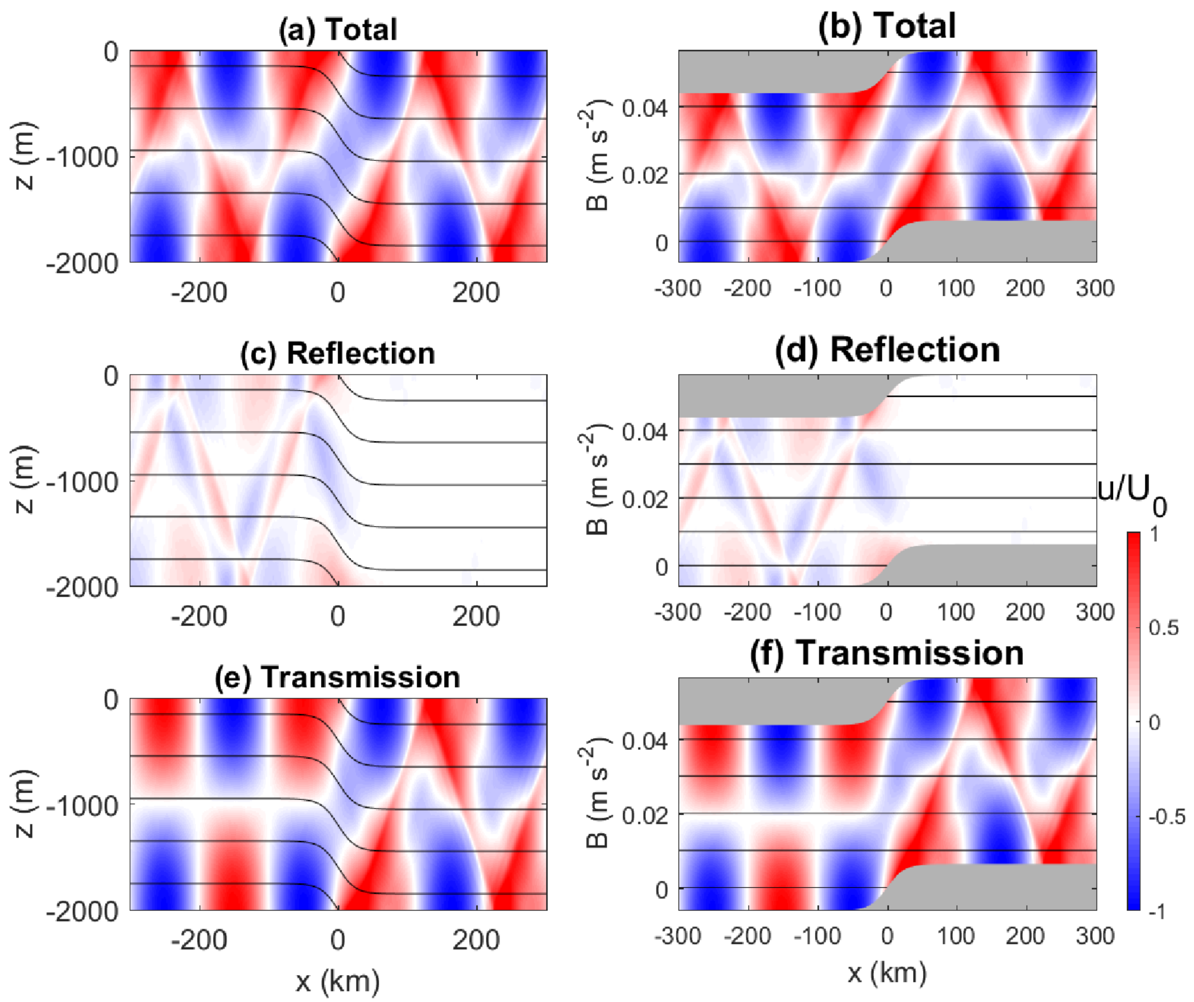


**Figure 3:** Rightward mode-one internal waves incident on a front at $x$=0. The total (top), reflected (middle) and transmitted (bottom) wave fields are plotted in the $z$ (left) and buoyancy $B$ (right) coordinates, respectively. Parameters of the internal waves and front are the same as Fig. 2a.

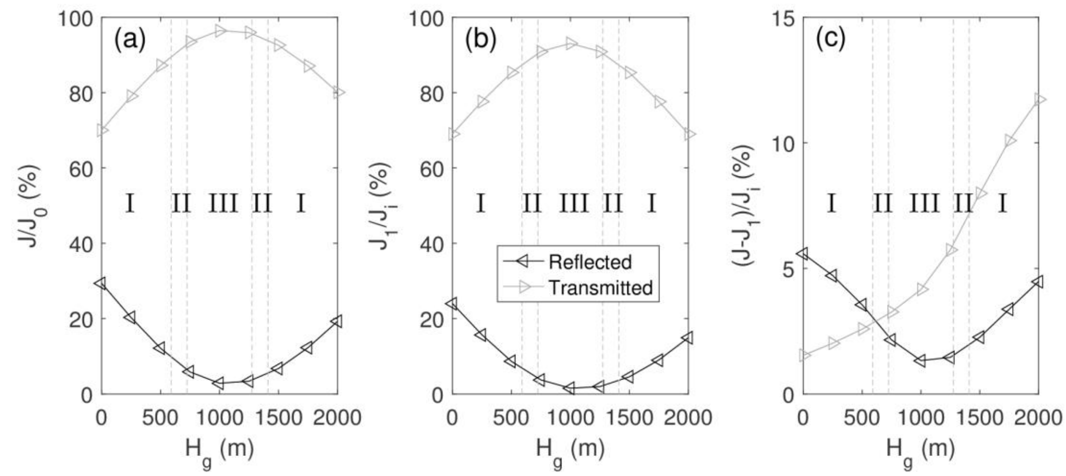


**Figure 4:** (a) Reflection and transmission coefficients for different levels of no motion $H_g$. (b) The energy-flux ratios between the reflected/transmitted mode-1 waves and the incident waves. (a) and (b) are similar because most reflection and transmission are in mode-one. (c) The energy flux ratio between the reflected/transmitted high-mode waves and the incident waves. Black for the reflected waves and gray for transmitted. $J_i$ represents the energy flux of incident waves and $J_r$ the energy flux of reflected waves. $J_{r1}$ is the energy flux for the mode-1 waves. I, II and III indicate the regimes defined in section 3.1. In this figure, front parameters $s = -0.01$, $N = 5\times10^{-3}$ $s^{-1}$ and $W = 25$ km.

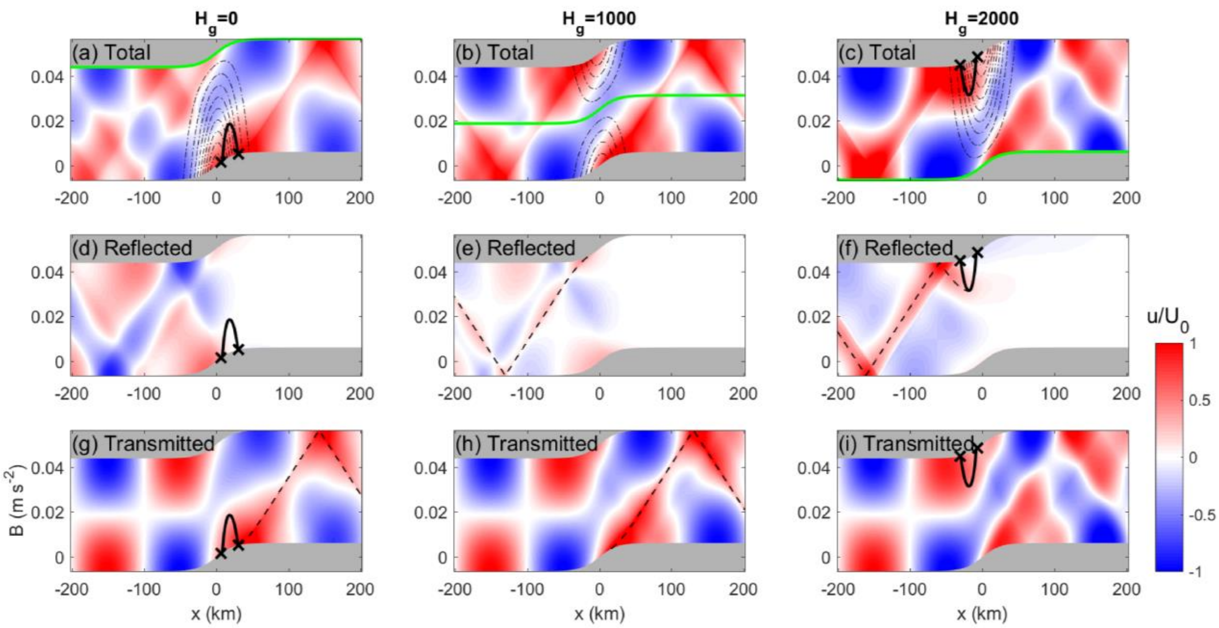


**Figure 5:** Wave fields (color) in buoyancy coordinates for mode-1 $M_2$ internal waves propagating across a geostrophic front. Top, middle and bottom panels show total, reflected and transmitted wave fields, respectively. Left, middle and right panels correspond to levels of no motion $H_g$=0 m, 1000 m and 2000 m, respectively. Black dashed lines show the ray paths. Black solid contours demark $\Delta$=0. In the top row, black dash-dot contours are the geostrophic flow $V$ with 0.5 m s-1 intervals and green solid curves indicate the reference level where $V$=0. Black crosses indicate the critical points on the bottom or surface boundaries. In this figure, $s = -0.01$, $N = 5\times10^{-3}$ $s^{-1}$ and $W$ = 25 km.

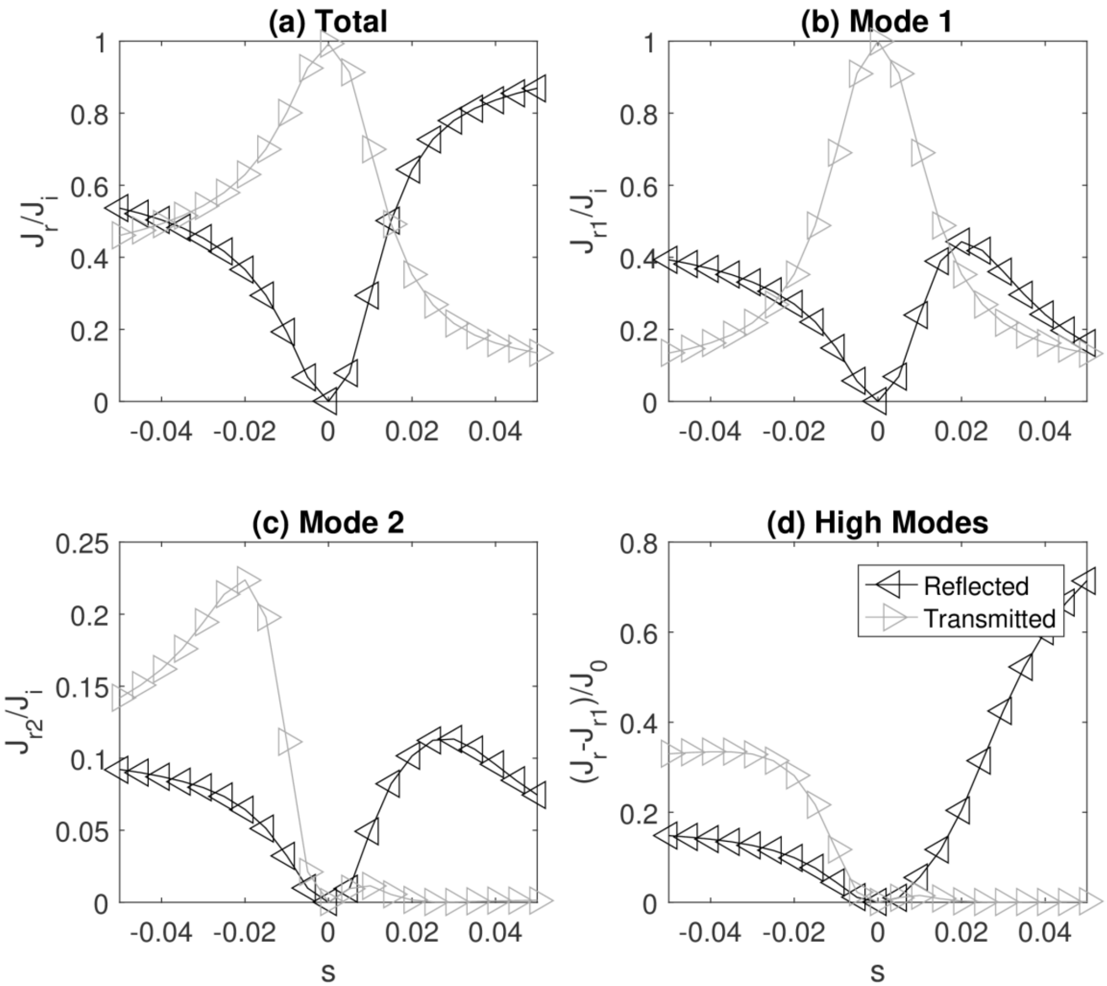


**Figure 6:** Energy flux ratios of reflected (black) and transmitted waves (gray) to the incident waves, as a function of isopycnal slope *s*, for (a) total, (b) mode-1, (c) mode-2 and (d) high-mode waves for $H_g$ = 2000 m, $N = 5\times10^{-3}$ s$^{-1}$ and $W$ = 25 km.

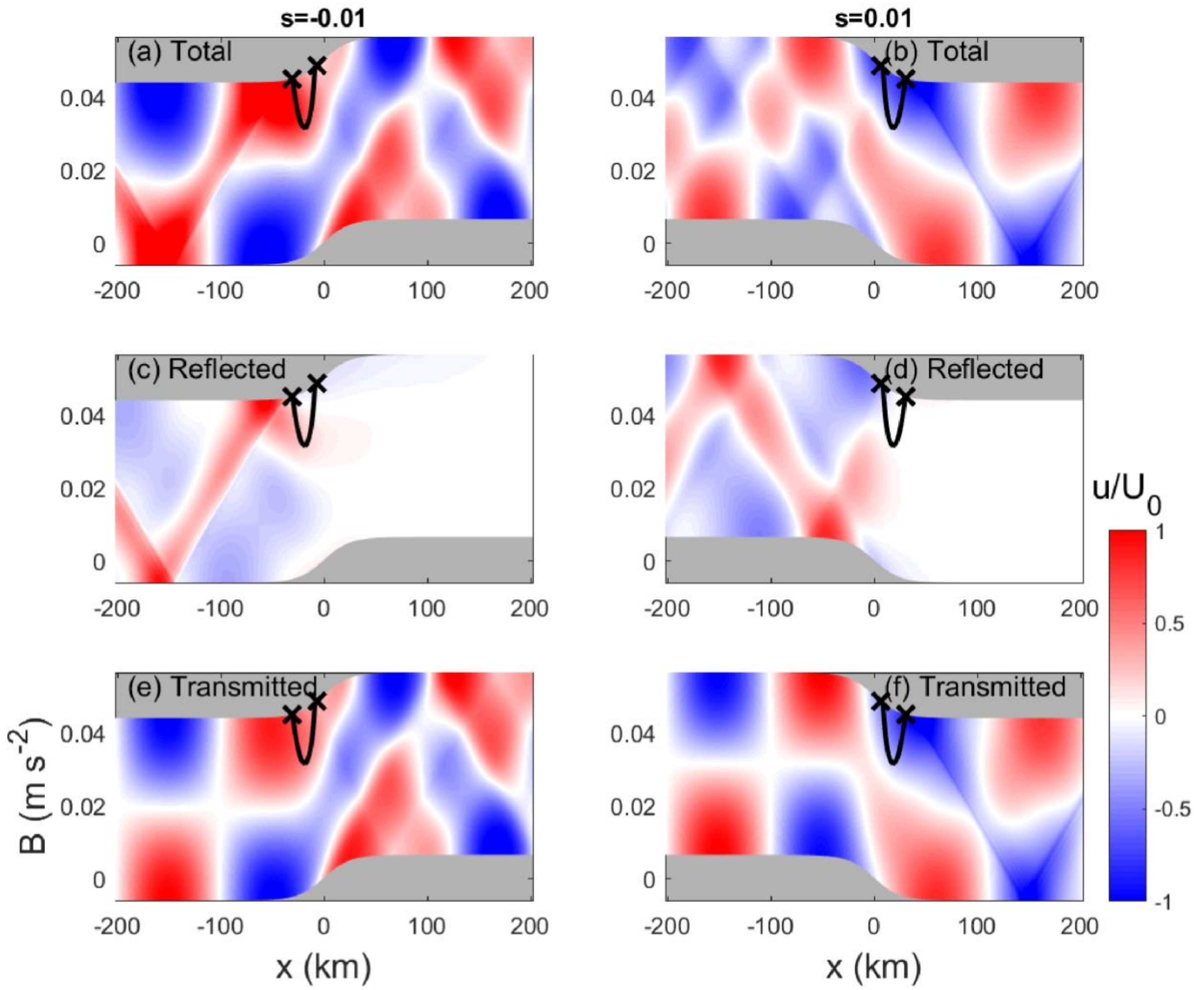


**Figure 7:** Wave fields for isopycnal slope *s*=-0.01 (left) and *s*=0.01 (right). Solid black contours demark $\Delta$=0. Black crosses indicate the critical points on the surface boundary. Front parameters are the same as Fig. 6.

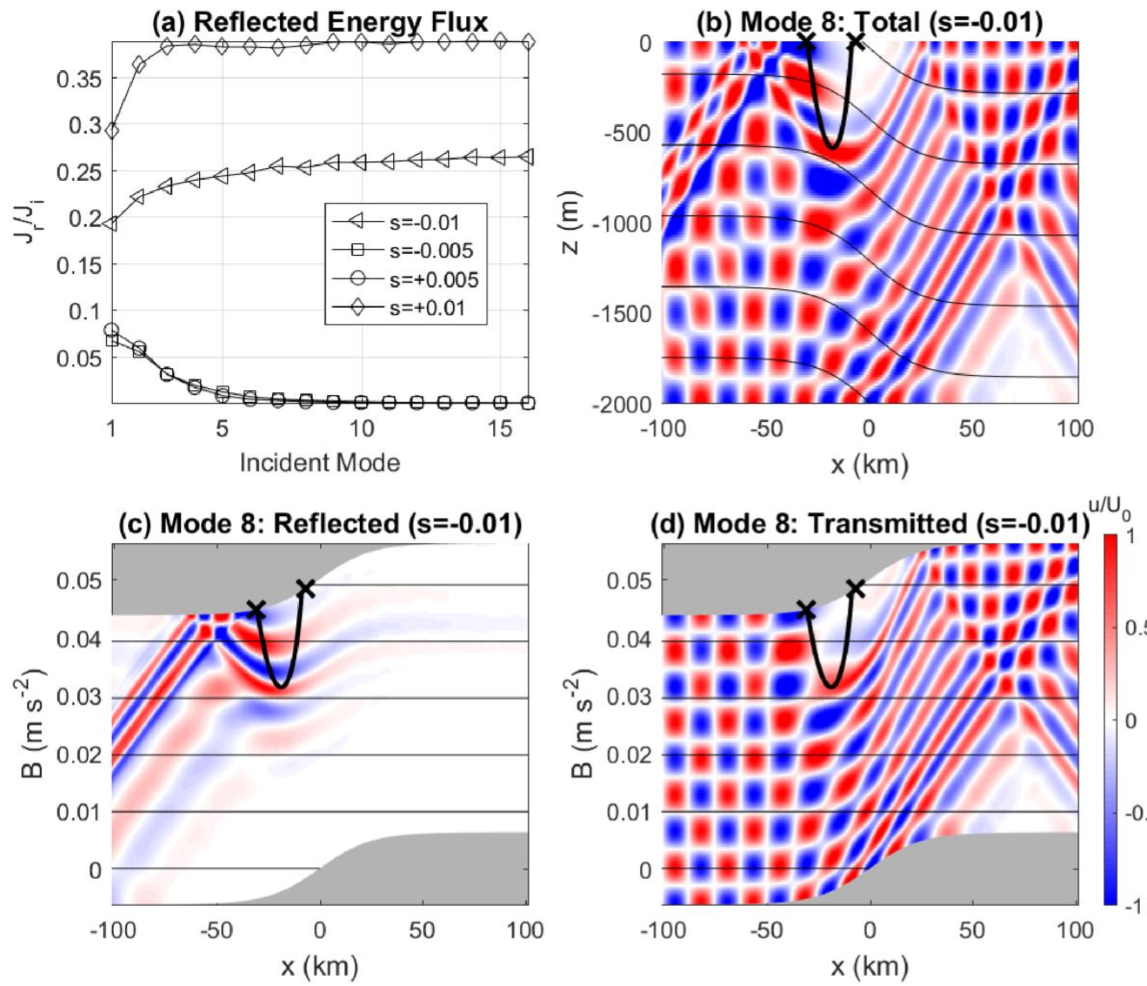


**Figure 8:** (a) $M_2$ reflection coefficients as a function of mode numbers for isopycnal slopes $s$=±0.005 and ±0.01. (b), (c) and (d) show the total, reflected and transmitted wave fields, respectively, for incident mode-8 $M_2$ internal waves for $H_g$ = 2000 m, $N = 5\times10^{-3}$ $s^{-1}$ and $W$ = 25 km. Bold black curves indicate the virtual boundary $\Delta$=0 and black crosses the critical slopes..

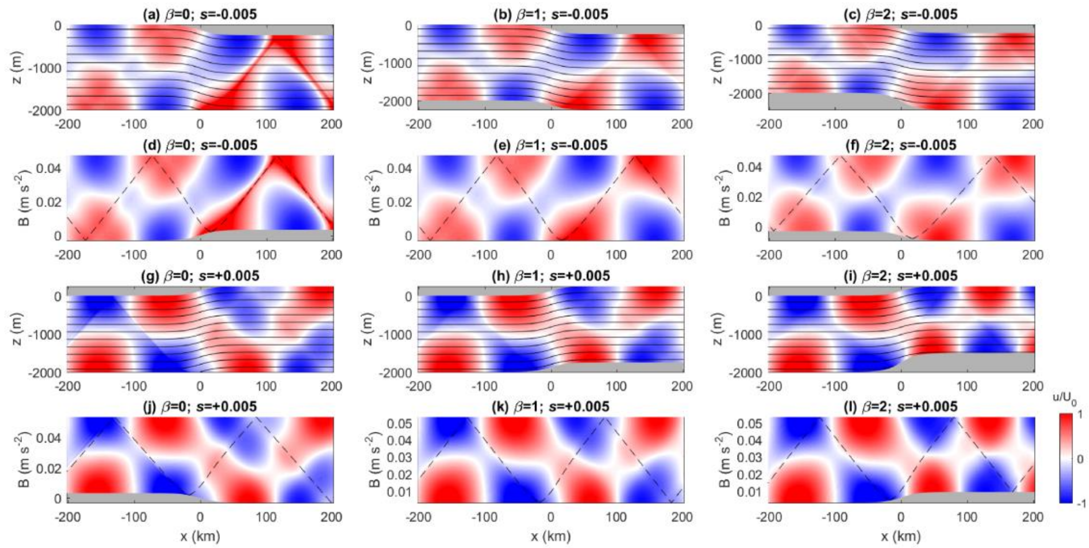


**Figure 9:** Wave fields for different topographic slope *β* and isopycnal slope *s* in Cartesian (rows 1 and 3) and buoyancy coordinates (rows 2 and 4) for $H_g$ = 2000 m, $N = 5\times10^{-3}$ s$^{-1}$ and $W$ = 25 km. Black contours indicate isopycnals in theCartesian coordinates. Red and blue indicate the normalized horizontal velocity *u* of internal waves.

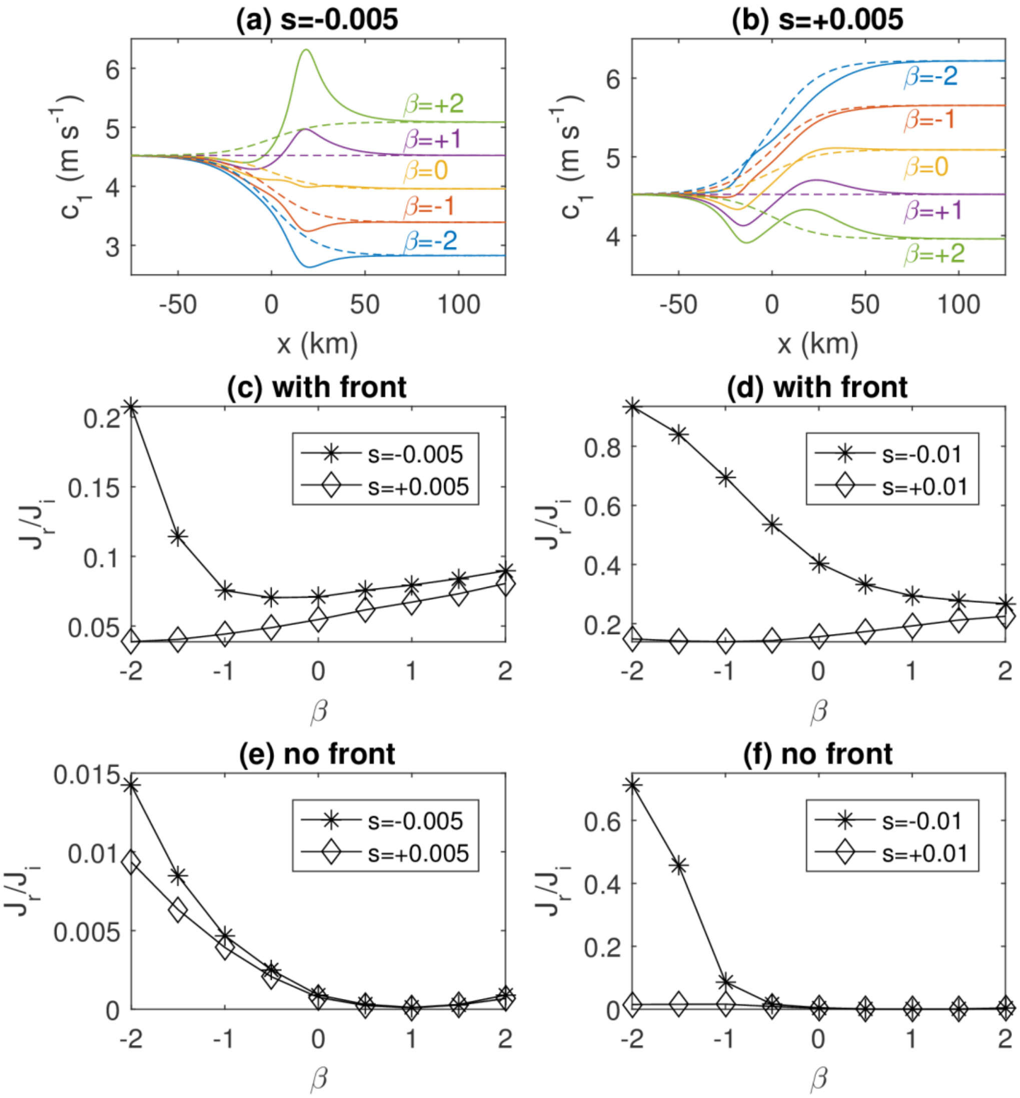


**Figure 10:** (a) and (b) show phase speed of mode-one $M_2$ internal waves across the front for isopycnal slopes $s$=±0.005, respectively. Bottom topography is defined in (38). $\beta$ is the ratio of bottom to isopycnal slope. (c) and (d) are reflection coefficients $J_r/J_i$ as a function of $\beta$ for $s$=±0.005 and $s$=±0.01. In (e) and (f), reflection coefficients are computed using the same bottom topography as in (c) and (d) but with horizontally uniform stratification. Front parameters are the same as Fig. 9.

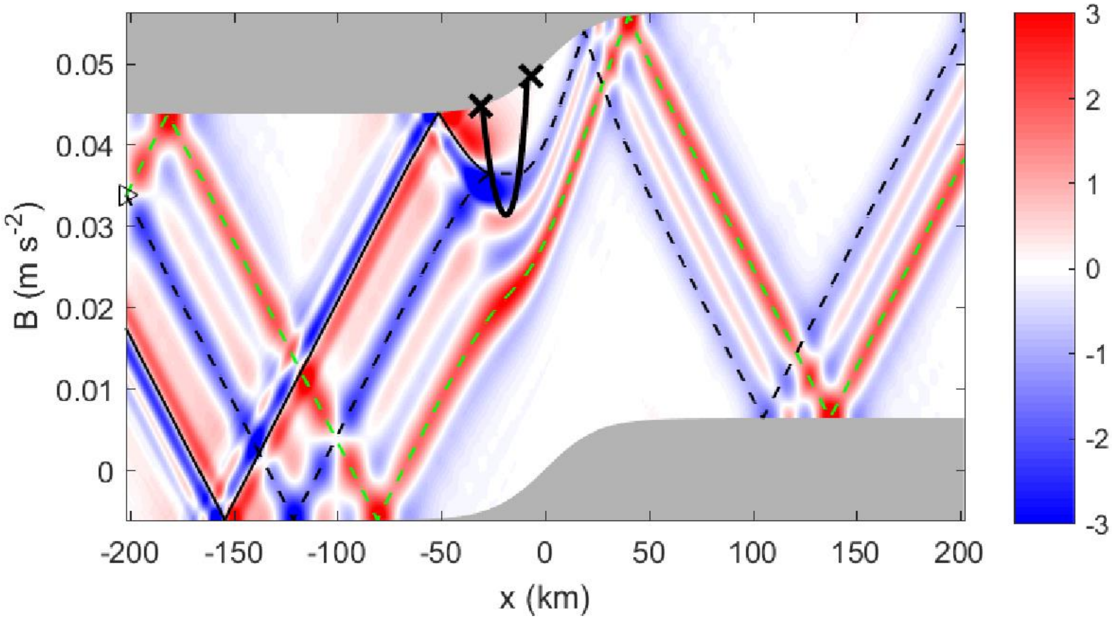


**Figure 11:** Horizontal velocity, $u/U_0$, for an internal-wave beam propagation across a geostrophic front for $s$ = −0.01, $H_g$ = 2000 m, $N = 5{\times}10^{-3}$ s$^{-1}$ and $W$ = 25 km in buoyancy coordinates. The incident ray originates from the black triangle on the west boundary. Bold black curves indicate $\Delta$=0 and black crosses the critical slopes. Three lines are superimposed to highlight ray propagation. Green and black dashed rays propagate across the front, but the black solid one reflects from the virtual boundary.

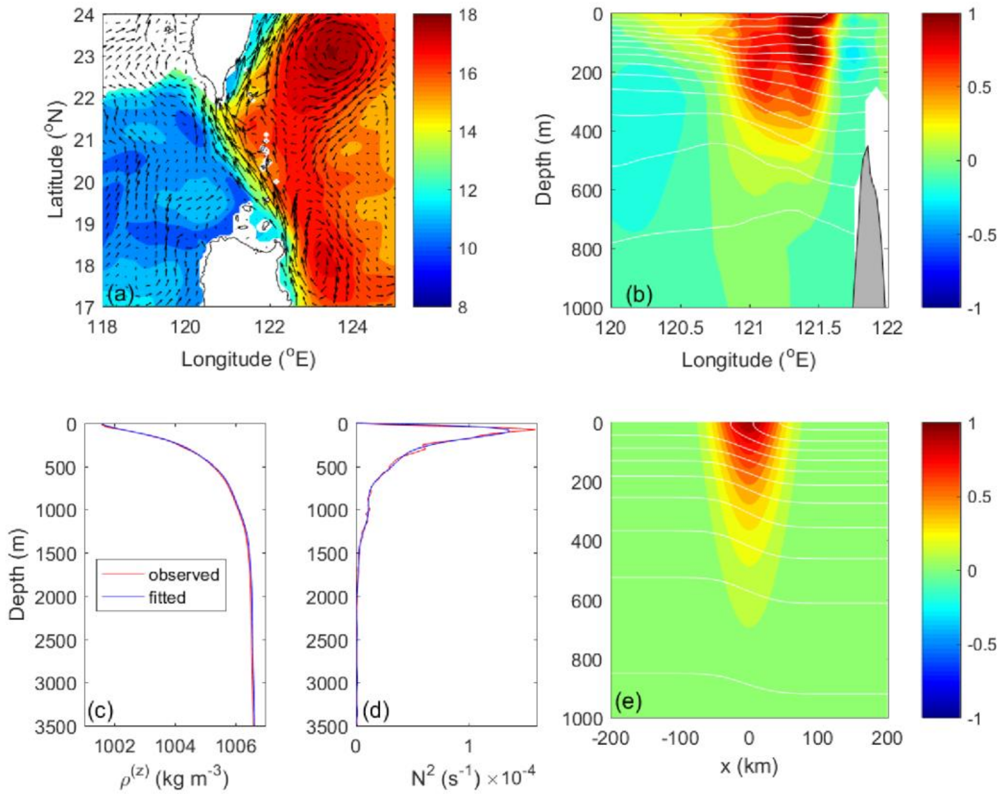


**Figure 12:** (a) Temperature at 500 m depth (color) and current velocity at surface on 5 August 2007 in the HYCOM model. (b) Temperature (white contours) superimposed on meridional velocity (color, m s$^{-1}$) for the upper 1000 m in HYCOM. Bottom topography averaged between 20°N and 21°N is shadedin gray, representing Heng-Chun Ridge. (c) and (d) show density and buoyancy frequency squared profiles, in which the red curves are averaged from CTD casts and the blue ones approximated using polynomial curve fitting. (e) Fitted temperature (contours) and meridional velocity (color, m s$^{-1}$) using (43) and (44).

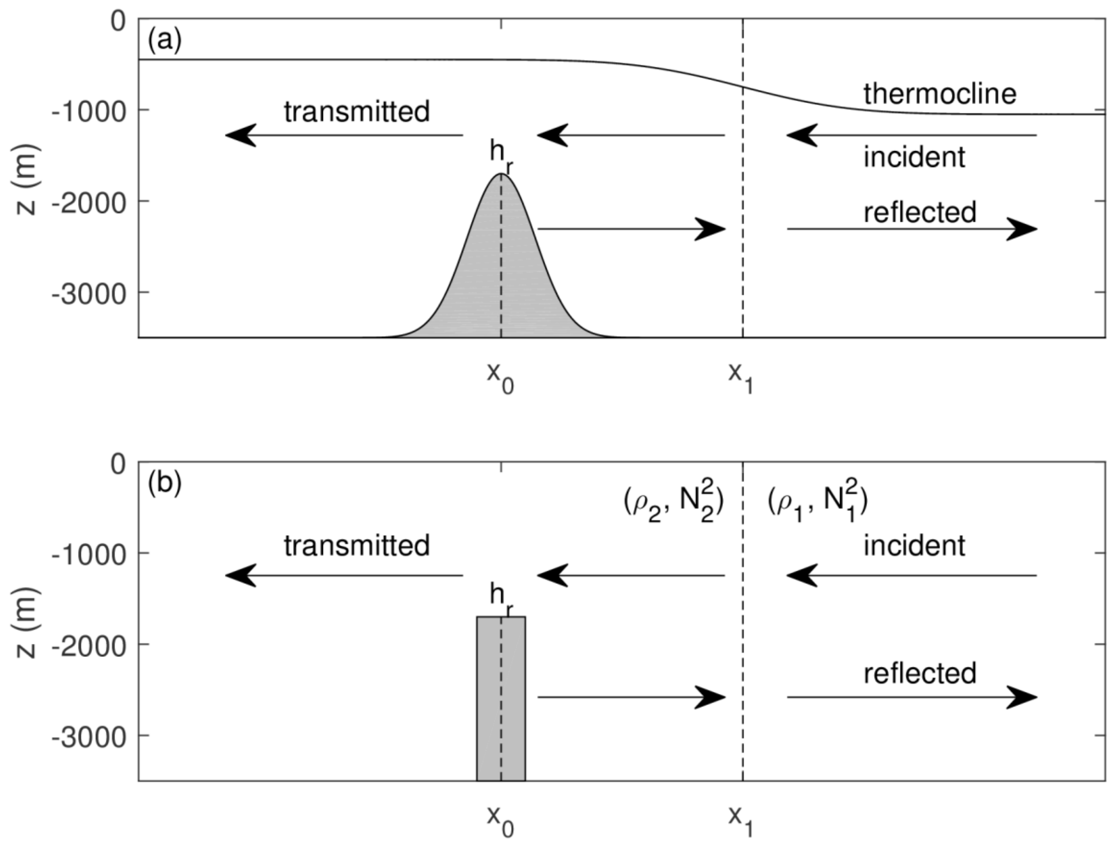


**Figure 13:** Schematics for models applied in Luzon Strait. Bottom topography is shaded in gray representing Heng-Chun Ridge. Incident waves come from the east. The top is for (12) and the bottom is for the simplified model. Arrows indicate directions of wave propagation. $x_0$ and $x_1$ indicate the locations of the ridge and front, respectively.

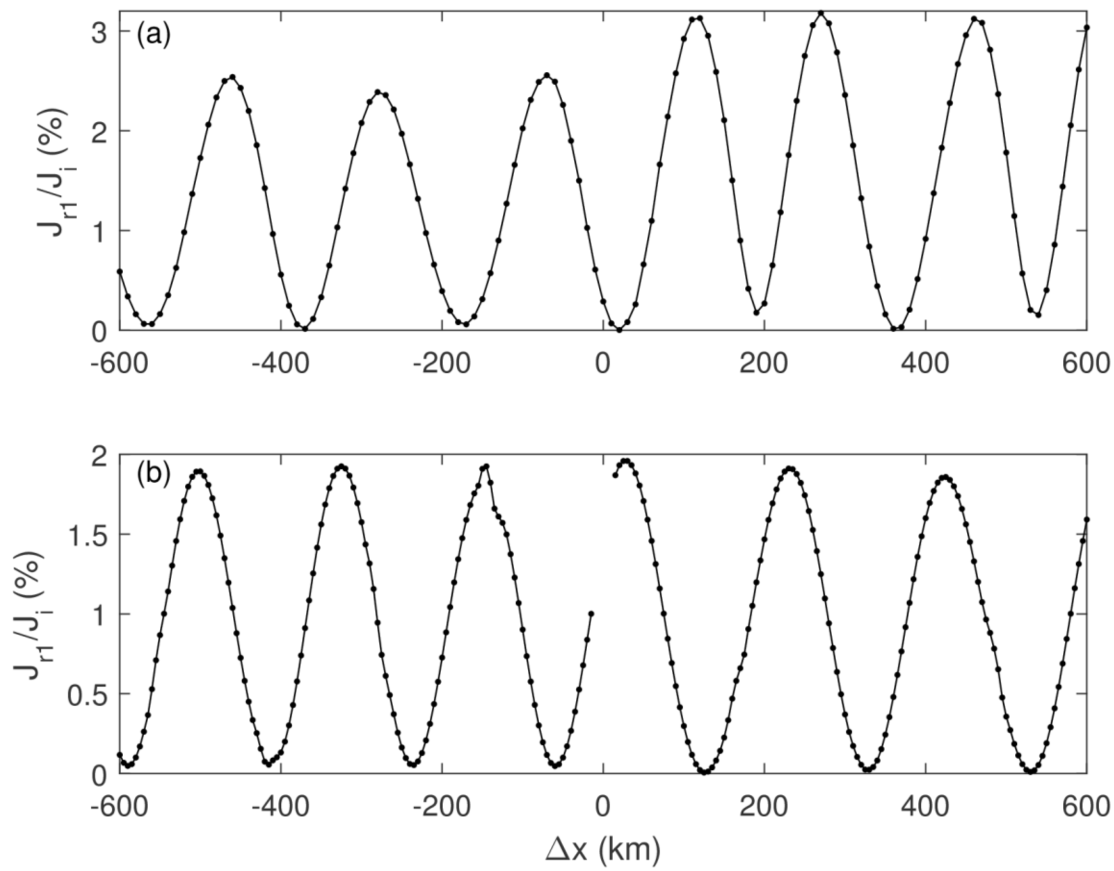


**Figure 14:** Reflection coefficients for $K_1$ mode-one internal tides propagating across the westerly Heng-Chun Ridge computed using (12) (a) and using the simplified model (b). $\Delta x = x_1 - x_0$ is the separation between the front and ridge shown in Fig. 13b. Data in (b) for $\Delta x \leq 10$ km are missing due to overlap between the ridge and interface between two stratifications, which cannot be resolved by the simplified model.

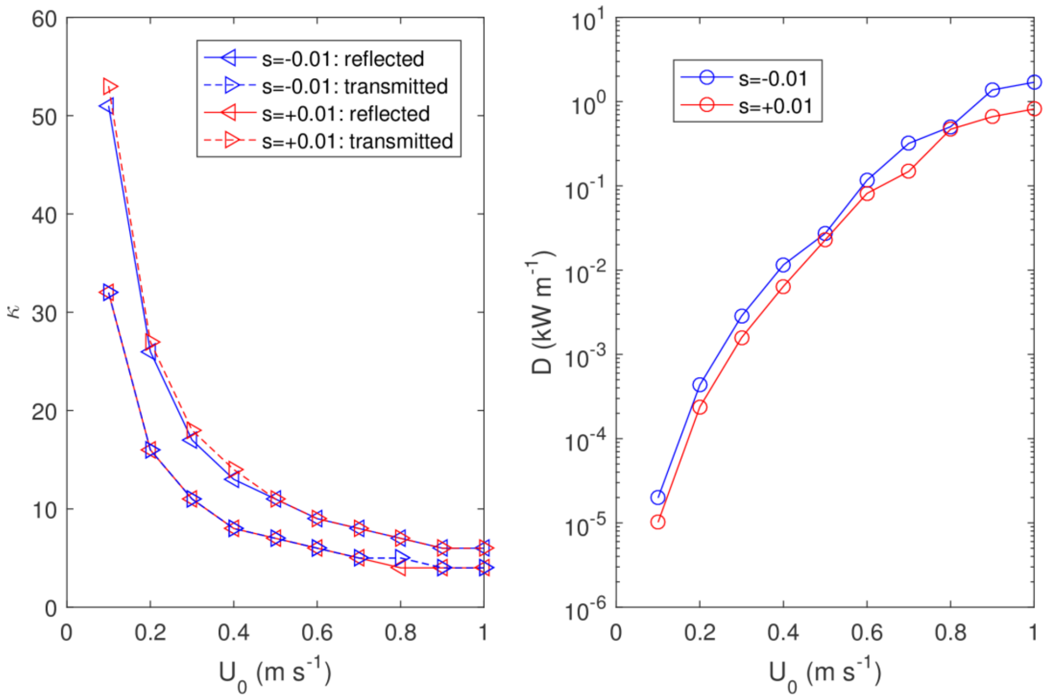


**Figure 15:** (a) Cutoff mode numbers $\kappa$ and (b) dissipation for different amplitude $U_0$ of incident mode-one $M_2$ internal waves with isopycnal slopes $s$=±0.01.